Patient-Motion Analysis in Perfusion Weighted MRI

Thesis submitted in partial fulfillment
of the requirements for the degree of

MS by Research
in
Computer Science and Engineering

by

ROHIT GAUTAM
200702035
rohit.gautam@research.iiit.ac.in

Centre for Visual Information Technology
International Institute of Information Technology
Hyderabad - 500 032, INDIA
January 2013

International Institute of Information Technology
Hyderabad, India

CERTIFICATE

It is certified that the work contained in this thesis, titled " Patient-Motion Analysis in Perfusion Weighted MRI " by Rohit Gautam, has been carried out under my supervision and is not submitted elsewhere for a degree.

_____ _____

Date Adviser: Prof. Jayanthi Sivaswamy

To

Mummy and Papa

Acknowledgments

Foremost, I would like to express my sincere gratitude to my advisor Dr. Jayanthi Sivaswamy for the continuous support of my research, for her patience, motivation, enthusiasm, and immense knowledge. Her guidance helped me in all the time of research and writing of this thesis.

Besides my advisor, I would like to thank Dr. Ravi Varma of K.I.M.S for his knowledge on the subject, human anatomy and guidance on the matters crucial to my research.

The research described in the thesis would not have been possible without a close collaboration to GE, India. I owe a great deal of appreciation and gratitude to Dattesh Shanbhag and Rakesh Mullick for providing me an internship opportunity and guidance on my research.

I thank my fellow labmates in MIP group for the stimulating discussions and feedbacks that contributed towards successful completion of my thesis. Also, I thank my friends for great support at required times and for all the fun we had in the past years.

Last but not the least, I would like to thank my family: my parents, my elder brother and elder sister who supported me and motivated me to never give up.

Abstract

Information about blood flow in the brain is of interest to detect the presence of blockages and ruptures in the vessel network. A standard way of gathering this information is to inject a bolus of contrast agent into the blood stream and imaging over a period of time. The imaging is generally done over an extended period of time (tens of minutes) during which a patient can move which in turn results in corruption of the acquired time series of volumes. This problem is often observed in dynamic magnetic resonance (MR) imaging. Correction for motion after scanning is a highly time-intensive process since it involves registering each volume to a reference volume. Moreover, the injected contrast alters the signal intensity as a function of time and often confounds traditional motion correction algorithms. In this thesis, we present a fast and efficient solution for motion correction in 3D dynamic susceptibility contrast (DSC) MR images. We present a robust, multi-stage system based on a *divide and conquer* strategy consisting of the following steps: i) subdivision of the time series data into bolus and non-bolus phases depending on the status of bolus in the brain, ii) 2D block-wise phase correlation for detecting motion between adjacent volumes and categorizing the corruption into four categories: none, minimal, mild and severe depending on the degree of motion and iii) a 2-pass, 3D registration consisting of intra-set and inter-set registrations to align the motion corrupted volumes. The subdivision of time-series into distinct sets is achieved using Gamma variate function (GVF) fitting. The dynamic non-uniform variation in signal intensity due to the injected bolus is handled by employing a clustering-based identification of bolus-affected pixels followed by correction of their intensity using the above GVF fitting.

The proposed system was evaluated on a real DSC MR sequence by introducing motion of varying degrees. The experimental results show that the entropy of the derived motion fields is a good metric for detecting and categorizing the motion. The evaluation of motion correction using the dice coefficient measure shows that the system is able to remove motion accurately and efficiently. The efficiency is contributed to by the proposed detection as well as the correction strategy. Including the detection prior to existing correction methods achieved a savings of 37% in computation time. Whereas, when the detection is combined with the proposed correction stage, the savings increase to 63%. Notably, the above performance was found to be had with no trade-off between accuracy and computation cost.

Contents

List of Figures

List of Tables

Chapter 1

Introduction

1.1 Stroke

Stroke is a rapid loss in brain function due to disturbance in blood supply to the brain. Disturbance is either in the form of an interruption to blood supply to a part of brain or a blood vessel rupture resulting in spilling of blood in nearby brain cells. In both scenarios, the brain cells do not receive the oxygen and nutrients travelling through blood and eventually die. When stroke is due to inadequate blood supply, it is termed as ischemic stroke which leads to infarction. It may occur either due to formation of a blood clot in a narrow artery (referred to as thrombotic stroke) or due to breaking of blood clot from some part of the body and travelling to the brain (referred to as embolic stroke). When stroke occurs due to bleeding into or around the brain, it is referred to as haemorrhagic stroke. People having defects e.g. aneurysm or arteriovenous malformation in blood vessels of the brain are prone to this kind of stroke. Figure 1.1 shows the two types of strokes and their effects on the human brain. The risk factor for stroke include high blood pressure, diabetes, family history of stroke, increasing age. The symptoms of stroke depend on the part of the brain that has been damaged. These symptoms include headache, unconsciousness, coma, changes in taste or hearing, loss of memory, difficulty in reading or writing etc.

1.2 Diagnosis of stroke

Usually there is a delay from the onset of symptoms to permanent tissue damage. When the blood flow to brain is interrupted, some of the brain cells die immediately while the other cells are at a risk of death. These type of cells make up the ischemic penumbra region [6] as shown in Figure 1.2. With timely diagnosis and treatment these cells at risk can be salvaged. Hence, an early diagnosis can help reduce mortality and morbidity of patients. This idea has led to advancements of new and effective methods for early diagnosis and treatment of stroke.

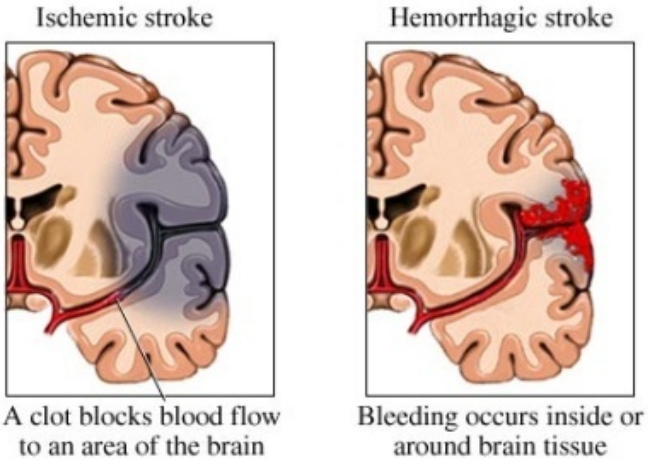

Figure 1.1 Effects of ischemic and hemorrhagic strokes in human brain [4].

Figure 1.2 Penumbra region in a stroke [1].

1.2.1 Computed Tomography (CT)

CT (computed tomography) scan uses X-rays to create three-dimensional image of the internal organs of human body including soft tissues, bones and blood vessels. CT produces a volume of data that is created from a large series of two-dimensional X-ray images of slices(cross-section) taken around a single axis of rotation. CT scan is most commonly used for diagnosis of acute stroke. It often shows the size and location of tumours, clots etc. CT scans are the basic methods of determining whether the stroke is ischemic (thrombotic or embolic) or haemorrhagic. If the stroke is haemorrhagic, the symptoms of bleeding into brain can be seen almost immediately using CT scan. The benefits of CT scan is that it is readily available at all centres and it is fast due to a short scan-time. There maybe several reasons for a stroke to not appear on a CT scan. In many cases, the the abnormality does not appear for the first several hours after the onset of stroke. Also, if the size of stroke region is very small or it is located in a region (cerebellum or brain stem) not imaged well by CT, it may not appear on the scan. Figure 1.3(a) shows an example of a CT image containing stroke.

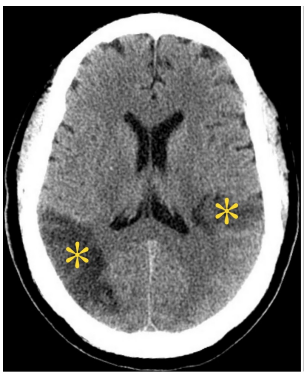

(a) CT scan with stroke.

(b) MRI scan with stroke

Figure 1.3 Slices taken from CT and MRI scans of brain affected by ischemic (thrombotic) stroke.

1.2.2 Magentic resonance imaging (MRI)

Magnetic resonance imaging(MRI) is an imaging method based upon the properties of water molecules which constitutes upto $70\% \sim 90\%$ of most tissues. The amount of water and its properties can change due to abnormalities which makes MRI very important for diagnosis purpose. It is able to detect very small changes in the magnetization of nucleus of atoms. MRI takes advantage of the fact that protons contained in water get aligned to a magnetic field. When a subject is inside a MRI scanner, the magnetic moments of the protons are aligned in the direction of the powerful magnetic field applied by the scanner(in range $0.2 \sim 3$ Tesla). A radio frequency (RF) current is then turned on for a short period of time producing a varying electromagnetic field. This field has resonance frequency that can change the spins of the protons in the external magnetic field causing them to alter their alignment with respect to the field. When the electromagnetic field is turned off, the spins of the protons restores to an equilibrium and the magnetization aligns with the applied magnetic field. During this relaxation period, the nuclei lose energy and emit a radio frequency signal known as free induction decay (FID) response signal. This signal is measured using receiver coils. The measurement is processed or reconstructed to obtain greyscale MR images.

MR consists of two characteristic times called spin-lattice relaxation time (T_1) and spin-spin relaxation time (T_2). Spin-spin relaxation is the mechanism by which the transverse component of magnetization vector decays to its equilibrium value of 0. In spin-lattice mechanism, the z-component of the magnetization vector comes in equilibrium with its surroundings. These relaxation rates depend on the type of tissue. The relation between various tissue types, their T_1 and T_2 values and their appearance in corresponding MR scans is shown in Table 1.1. Fluids have long T_1, water based tissues have a moderate value and fat-based tissues have short T_1. For a given tissue, T_2 is shorter than T_1. The contrast in MRI images depend on T_1 and T_2. In T_1-weighted MR images, tissues with the longest T_1 give the weakest signal, hence the bright pixels belong to tissues with short T_1. On the other hand, in T_2-weighted MR images, tissues with longest T_2 give strongest signal intensity. There are two types

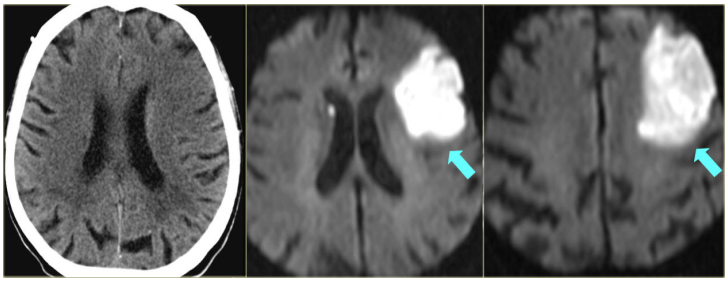

Figure 1.4 CT and diffusion MR images of a patient suffering from stroke. [1].

Table 1.1 T_1 and T_2 values of different types of tissues and their appearance in corresponding MR scans.

Tissue Matter	**T_1 value**	**Appearance in T_1 scan**	**T_2 value**	**Appearance in T_2 scan**
Fluids	High	Dark	High	Bright
Water	Medium	Mid-grey	Medium	Mid-grey
Fat-based	Low	Bright	Low	Mid-grey

of pulse sequences associated with MRI, called spin echo (SE) and gradient echo (GE). SE sequences use two RF pulses to create echo which measures the signal intensity [11]. They produce high quality images but take a relatively large amount of time - several minutes. GE sequences use single RF pulse followed by a gradient pulse for measuring signal intensity. They have shorter scan times as compared to SE sequences. However, they are affected by the applied magnetic field which affects T_2. This is referred to as T_2^*.

CT scans are currently the standard test used for diagnosis of stroke. However, it has been found that MR scans are better at detecting acute ischemic stroke as compared to CT scans [15]. An example of this is diffusion MR scan. Diffusion MRI is considered more useful as compared to CT for diagnosis of ischemic stroke within 12 hours of onset. Diffusion MRI measures water flow in tissues. In a stroke affected region, diffusion of water molecules is restricted. Hence, the affected region gets identified easily. Some specific MRI scans show the severity of stroke. They are also able to detect the stroke earlier as compared to CT. Figure 1.4 shows the difference between CT and diffusion MR images of a patient affected by ischemic stroke. From the figure, it can be seen that using diffusion images, the infarction can be detected easily. This is why, diffusion images are often referred to as stroke sequence. Hence MRI is a better choice as compared to CT from stroke diagnosis. On the other hand, MRI is not readily available at all centres and the scan time for MRI is longer than CT. Hence, MRI cannot be used if it causes a significant amount of delay in the diagnosis. Figure 1.3(b) shows an example of a MRI scan containing stroke.

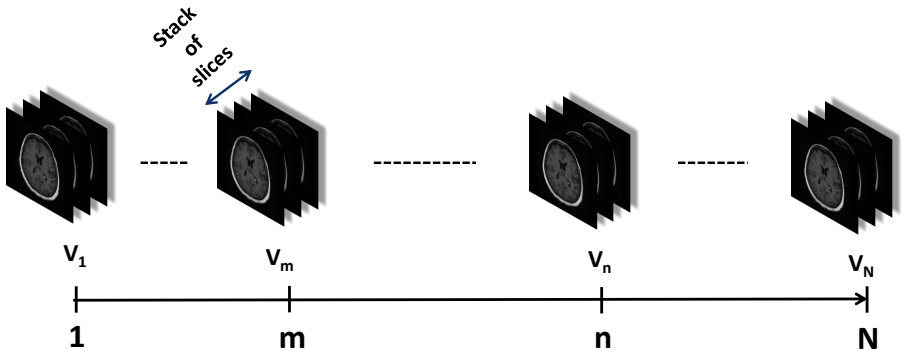

Figure 1.5 An example of a perfusion time-series with volumes acquired at discrete time-points in range [1, N]. Each slice is of dimension 128×128. Stack of slices constitute a volume. Each volume is a matrix of dimension 128×128×20. In a typical perfusion time-series, no. of volumes acquired ranges from 25-50.

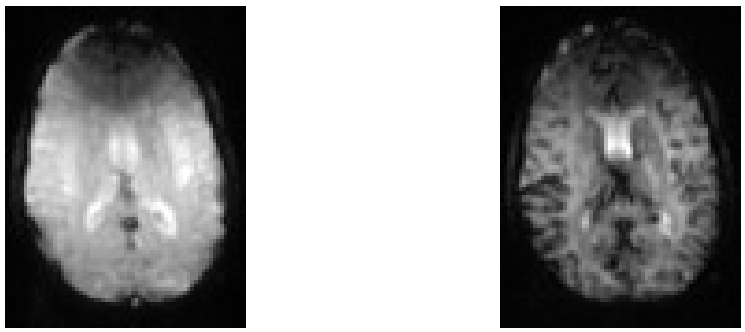

(a) Normal slice **(b) Bolus affected slice**

Figure 1.6 Two slices taken from a 3D perfusion MRI time-series. Notice the change in image intensity in localised manner in (b) due to presence of bolus.

1.3 Perfusion MRI

Advancements in MRI has led to diffusion and perfusion MRI for diagnosis of acute ischemic stroke. In the context of MRI, diffusion refers to the motion of water molecules while perfusion refers to the observation of blood flow through an organ [55][19]. In perfusion MRI, an exogenous paramagnetic contrast agent (bolus) is injected into the blood stream of patient and it is tracked in the brain by acquiring 3D time series MRI [21][40]. Hence, perfusion MRI is often termed as bolus tracking. Once the time-varying data is obtained, it is parametrized at a voxel-by-voxel basis using various physiological models to obtain various hemodynamic indices, like relative cerebral blood flow(rCBF), relative cerebral blood volume(rCBV), relative mean transit time (rMTT). These indices help profile the blood flow characteristics in different tissues which is needed in detection of various disease states and deciding treatment options. Perfusion measurements with MRI is also used in other areas like tumour characterization and progression, determining salvageable tissues in stroke post acute ischemic event in brain, inflammation and infectious diseases.

1.4 Data corruption due to subject motion in perfusion MRI

A disadvantage associated with MRI in comparison to other imaging modalities, e.g. X-rays, CT is the relatively large image acquisition time. A single MRI scan takes $1 \sim 10$ minutes. In perfusion MRI, a 3D time-series is acquired as shown in Figure 1.5. Thus, depending on the number of repeated scans, the total scan-time of a perfusion series can lie in the range $20 \sim 60$ minutes. Due to such a large image acquisition time, it becomes difficult for patients to remain still for the entire scan period. If the patient moves during scanning, the image quality is degraded. This kind of problem arises especially when MRI scans are conducted for young children or the patient is claustrophobic or the patient is suffering from mental illness. Sedation can minimize the risk of patient motion during image acquisition but it is not feasible in all cases, e.g. patient with medical condition due to sedation or due to the risks involved with sedation. Different mechanical attempts have been made to limit patient motion such as placing padding around subject's head but these methods are not fail-safe.

In perfusion MRI, accurate measurement of perfusion parameters relies on tracking the signal in a particular voxel which is compromised due to patient motion. This motion causes intervolume mis-alignments and mixing of signals from neighbourhood tissues. Consequently, the perfusion parameters generated from this data become inaccurate. Thus the problem of data corruption due to patient motion in perfusion MRI is severe in nature.

Traditional approach to solve the data corruption problem in perfusion MRI is via 3D registration on acquired MR images. However, in perfusion MRI, the problem is compounded by the localised changes in intensity of acquired MR scans due to injected bolus as shown in Figure 1.6. Blood is delivered to different regions in brain through blood vessels, hence the effect of bolus present in blood is seen in those regions. This phenomenon brings out a local change in image intensity in different regions in a MR image. The concentration of bolus present in brain region also changes with time. Consequently, the localised change in image intensity (which depends on the concentration of bolus) takes place in a non-uniform manner with respect to time. Thus, the problem of data corruption becomes three-fold due the following transformations present in acquired perfusion MR images:

- global transformation (due to patient motion).
- a local change in image intensity (due to injected bolus).
- non-uniform nature of intensity variation (due to varying concentration of bolus in brain region).

A simultaneous occurrence of all the above three phenomena in perfusion MRI affects the traditional image analysis methods and cause them to perform poorly.

1.5 Problem statement and contributions

This thesis documents a method aimed at solving the problem of data corruption due to patient motion in perfusion MR scans. A fast and efficient multi-stage motion correction system based on divide and conquer strategy has been proposed. This thesis documents the following contributions:

- A fast method for detection of motion among perfusion MR scans has been proposed. The method reduces the number of volumes needed to be corrected for motion. Consequently, this reduces the overall time required for motion correction. Depending on the degree of patient motion, the acquired scans are characterized into one of the four motion categories: no, minimal, medium and severe motion categories.

- An efficient two-pass motion correction strategy for alignment of motion corrupted volumes has been proposed. Depending on the status of bolus in brain, the time-series is divided into distinct sets. In the first pass, intra-set alignments are performed. In the second pass, inter-set alignments are performed to correct for motion in the entire perfusion time-series.

1.6 Organisation

Introduction to the problem of data corruption in perfusion MRI and objective of the thesis is explained in Chapter 1. In Chapter 2, different perfusion parameters and the effect of patient motion on these parameters is discussed. In Chapter 3, we discuss existing approaches to motion correction in perfusion MRI. Later, we propose a divide and conquer strategy based system that is able to overcome the shortcomings of existing methods. In Chapter 4, we discuss the various stages in a perfusion MRI time-series depending on the status of bolus and also propose a method to divide the time-series into these stages. The detection of motion corrupted volumes and their characterization, are discussed in Chapter 5. We also show the experiments conducted, motion detection and characterization results. Chapter 6 talks about the correction of motion corrupted volumes and shows motion correction results. The application of the proposed system, its pros and cons and future prospects for the current system are discussed in Chapter 7.

Chapter 2

Patient motion analysis in Dynamic Susceptibility Contrast (DSC) MRI

MRI has become an important tool to for the study of human brain anatomy. Advancements in MRI has helped in evaluation and assessment of numerous metabolic and functional parameters that assist in diagnosis of diseases. Cerebral perfusion is one of these parameters that describes the blood flow through brain's vascular network. Cerebral perfusion MRI is commonly studied using T_2^*-weighted dynamic susceptibility contrast (DSC) imaging or T_1-weighted dynamic contrast enhancement (DCE) imaging. In this thesis, a system for motion correction in DSC-MRI is presented. The data acquired is a 3D DSC-MRI time-series. The images acquired in MRI are in form of slices. These slices are stacked on top of one another to form a 3D volume. The basic unit of a volume is called voxel that is analogous to a pixel in an 2D image. The volumes are acquired across a period of time to obtain a DSC-MRI time-series. Once the data is acquired, it is analysed at a voxel-by-voxel basis by the physicians and different perfusion parameters are obtained that help decide the status of disease in a patient. If there is relative motion among acquired volumes, the tracking of a voxel across time-points will be difficult. The perfusion parameters obtained from such a data will be inaccurate and result in a wrong diagnosis of the patient. In this chapter, we first explain the theory behind DSC-MRI. Later, we explain different perfusion parameters associated with DSC-MRI, the estimation of these parameters and then discuss the effect of patient motion on some of these parameters.

2.1 Dynamic Susceptibility Contrast (DSC) MRI

DSC-MRI aids non-invasive invivo diagnosis of a subject. It is based on the usage of susceptibility contrast induced by gadolinium based contrast agents [55] which helps in measurement of parameters during the first-pass of contrast agents in brain [7][46][45][47]. Paramagnetic substances in the bolus distort the magnetic field due to the presence of large magnetic moments and dipole-dipole interactions. These affect the T_1 and T_2 relaxation times of magnetisation. The change in tissue contrast due to increase in T_2 relaxation time is called susceptibility contrast. The contrast agents that are commonly used are gadolinium or dysprosium applied to a ligand molecule like diethylenetriaminepentaacetic acid

(DTPA).

In cerebral perfusion, hemodynamic parameters for different tissue regions are derived from MR images. These parameters (as we will see further) depend on the concentration of contrast agent present in the tissue regions. Thus, for a given MR image sequence, the relationship between observed signal intensity and contrast agent concentration must be understood. The relationship between contrast agent concentration and relaxation rates(T_2/T_2^*) of magnetization has been found to be approximately linear and is given by [40]:

$$\Delta R_2(t) \propto C_t(t) \tag{2.1}$$

where, R_2 is the relaxation rate change and $C_t(t)$ refers to the contrast agent concentration. After the contrast agent has been administered, the signal intensity change has been found to be dependent on transverse and longitudinal relaxation rates ΔR_2 and ΔR_1 and is given by [40]:

$$S(t) = S(t_0)(1 - exp^{TR.\Delta R_1(t)}).exp^{TE.\Delta R_2(t)} \tag{2.2}$$

where, $S(t_0)$ is the baseline signal intensity, TR and TE are repetition and echo times respectively. On combining Eq.2.1 and Eq.2.2, the relation between concentration of contrast agent and signal intensity is found as:

$$C_t(t) = -k.log\frac{S(t)}{S(t_0)}/TE \tag{2.3}$$

where k is proportionality constant which depends on tissue, the contrast agent, the magnetic field strength, and pulse sequence parameters. Using Equation 2.3, the concentration of contrast agent in various tissue regions can be estimated from acquired DSC-MRI time-series. Since the contrast agent concentration represents the amount of blood flow in various tissue compartments, this helps the doctors to know whether a tissue region is healthy or affected.

In DSC-MRI, as the contrast agent passes through a region, it induces susceptibility changes due to its paramagnetic properties. This results in shorter T_2^* values and a significant signal loss. This signal loss causes a reduction in the intensity giving a darker appearance to regions affected by contrast agent. The concentration of contrast agent that induces signal loss is proportional to the amount of blood flow in that region. Hence, if an area is affected by infarct, there will be no blood flow and consequently no drop in MR signal will be observed.

Figure 2.1(a) shows an example of a typical DSC-MRI time-series data. The corresponding mean-intensity profile ($\mu(n)$) is shown in Figure 2.1(b).

$$\mu(n) = \frac{1}{XYZ}\sum_{i=1}^{X}\sum_{j=1}^{Y}\sum_{k=1}^{Z}F_n(i,j,k)$$

where, F_n denotes the n^{th} volume (resolution $X \times Y \times Z$) in the time-series. From Figure 2.1(b), it can be seen that as the contrast agent washes into the brain region (at time-point n=10), a net drop in signal

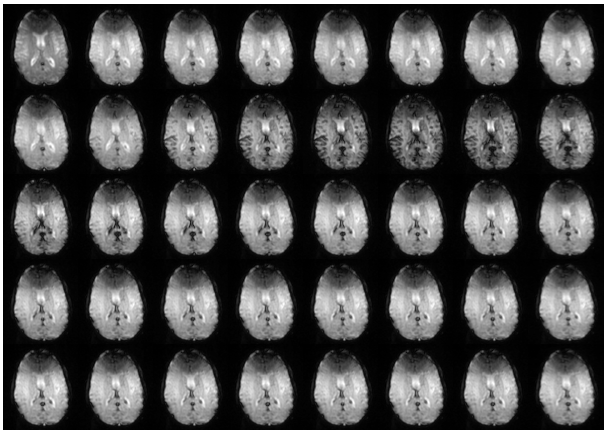

(a) a normal DSC-MRI time-series.

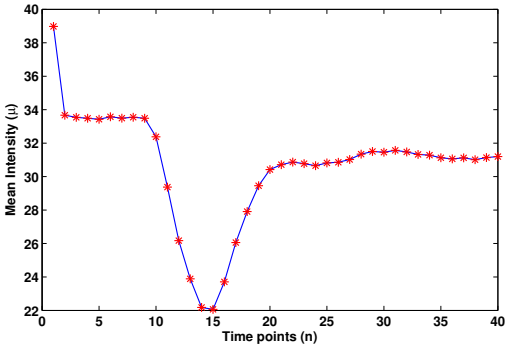

(b) Mean intensity profile.

Figure 2.1 Central slices of volumes in a DSC-MRI time series with mean intensity profile $\mu(n)$. (Mean-intensity refers to the mean-intensity of a volume.)

intensity is observed (called the first-pass of contrast agent). The susceptibility effect of the contrast agent is observed now. A non-uniform variation in signal intensity is observed after time-point n=10 due to change in contrast agent concentration in the brain region. From the moment of the entrance of bolus in brain region (wash-in of bolus), the concentration of bolus first increases upto a maximum value and then starts decreasing (wash-out of bolus). The mean signal intensity of the volumes varies with the concentration of bolus accordingly.

After the data has been acquired, different perfusion maps relating to the amount of blood flow in various regions are generated. These maps aid in making decision if the brain is affected. In the next section, we discuss important perfusion parameters.

2.2 Important perfusion parameters and their estimation

2.2.1 Cerebral Blood Volume (CBV)

When perfusion studies started, cerebral blood volume (CBV) became the first parameter used in studying blood flow in a region. CBV maps are derived by kinetic analysis of concentration time curves [47]. CBV indicates the amount of contrast agent (hence blood) that has passed through a region, assuming all of the contrast agent has passed through this region. Therefore, this parameter is used to identify the core region in infarcted tissue. The curve between change in concentration of contrast agent with time indicates the amount of concentration agent that has passed through the region. Since the contrast agent is contained in blood, the parameter indicates the amount of blood delivered to a region of interest in brain. Hence, CBV can be found by calculating the area under the concentration time curve. It is defined as the ratio of the areas under the curves corresponding to concentration of contrast

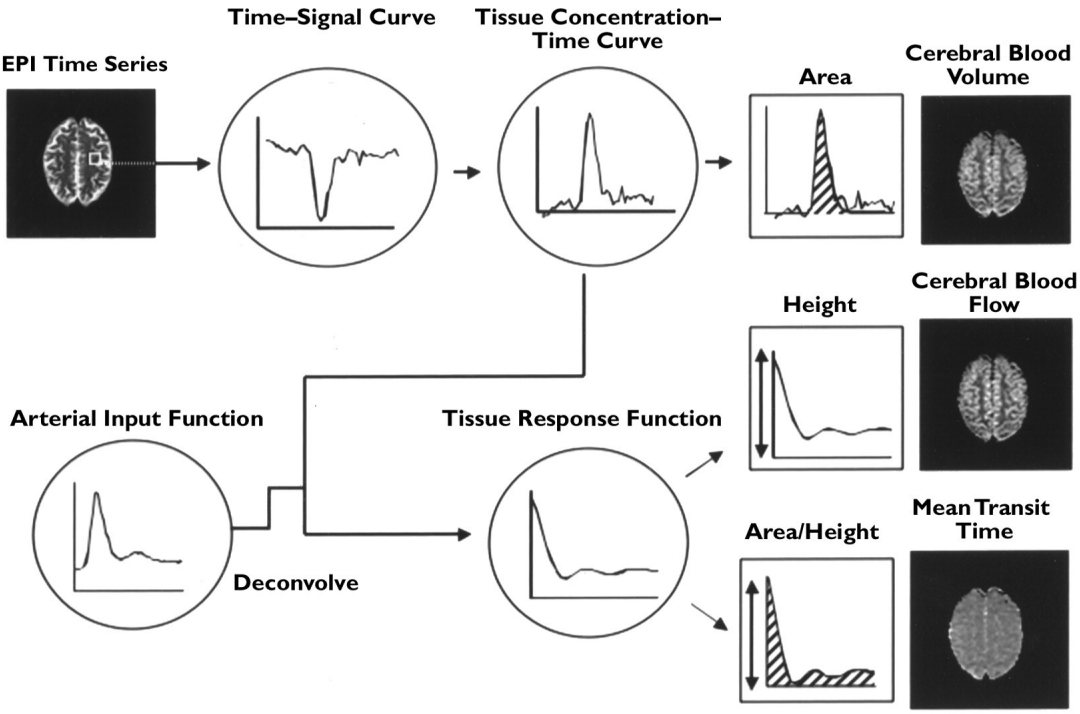

Figure 2.2 An overview of estimation of various perfusion parameters using obtained signal-time curves and derived concentration-time curves[42].

agent in tissues and arteries [36]:

$$CBV = \frac{\int_{-\infty}^{\infty} C_t(\tau)d\tau}{\int_{-\infty}^{\infty} C_a(\tau)d\tau}$$

where, $C_t(\tau)$ is the tissue concentration and $C_a(\tau)$ is the arterial concentration of contrast agent. It is measured in terms of volume of blood flowing through a region in millilitres per 100 grams of brain tissue (ml/100gm).

2.2.2 Cerebral blood flow (CBF)

The amount of perfusion in a tissue is often studied using another parameter called cerebral blood flow (CBF). This parameter is used to identify the penumbra region in a stroke. It refers to the amount of contrast agent, hence the blood supplied to a region of interest in a given time. In an adult, this value is $\sim$50 millilitres of blood per 100 grams of brain tissue per minute. The calculation of CBF requires knowledge of arterial input function (AIF) of contrast agent. Ideally, the AIF is an impulse function -

all the contrast agent should appear at a region of interest at a time-point and then disappear. Since it takes time to inject the contrast agent, and mixing of contrast agent with blood, the AIF is usually a bell-shaped function. The tissue concentration of contrast agent can be described by an arterial input function (AIF), R(t). The tissue concentration ($C_t(t)$) is given by:

$$C_t(t) = CBF.C_a(t) * R(t)$$

where, C_a is the arterial concentration of contrast agent and * denotes convolution. Using deconvolution methods, CBF can be estimated from the above equation. An estimate of CBF gives a measure of the amount of blood flow in a tissue. Since CBF value remains constant for a tissue type, an abnormal value of CBF shows that the region is affected.

2.2.3 Mean Transit Time (MTT)

Mean transit time (MTT) is the average time taken by blood or the contrast agent to reach a region of interest in brain. By the central volume theorem[50]:

$$MTT = \frac{CBV}{CBF}$$

It is measured in minutes. Similar to CBF, this parameter is used to identify the penumbra region in a stroke.

2.2.4 Time to Peak (TTP)

The concentration of contrast agent in a region varies non-uniformly. It increases from wash-in time-point until it attains a maximum and then reduces until it washes-out of the brain region. Time to peak (TTP) is the time-point in the concentration-time curve at which the concentration of the contrast agent in the tissue becomes maximum in the region of interest. It is measured in seconds.

Figure 2.2 gives an overview of the method by which different perfusion parameters are calculated using the obtained time-signal curve. The time-signal curve is converted to tissue concentration curve. The convolution of AIF and concentration-time curve is used to estimate these parameters.

Patient motion affects the accurate estimation of perfusion parameters which could lead to incorrect diagnosis. In the following section, we illustrate the effect of patient motion on perfusion parameters.

2.3 Error analysis of perfusion parameters with degree of motion

We illustrate the effect of subject motion on perfusion parameters by estimating various perfusion parameters on a given DSC-MRI dataset. Perfusion weighted MR imaging is rarely done in Indian hospitals, as it requires specialized expensive accessories. Hence, getting real patient-motion perfusion MR

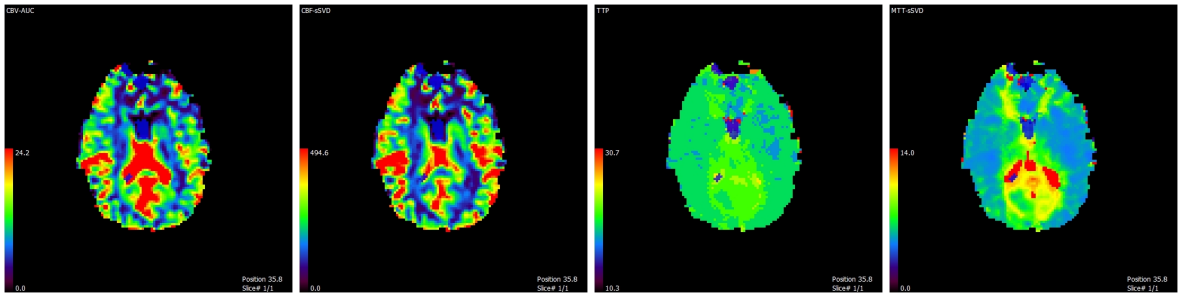

(b) **CBV** (c) **CBF** (c) **TTP** (c) **MTT**

Figure 2.3 Different perfusion maps estimated from DSC-MRI data.

data was impossible. The data we used was obtained from KIMS as part of a research project done earlier for a tumour study. In our experiments, simulated motion was applied to this real perfusion data. For validating the proposed method, a set of experiments were performed. Known amount of 3D-rotation was added to the volumes to simulate actual patient motion during DSC-MRI scan, in consultation with a neuro-radiologist. A number of consecutive volumes at repeated intervals in the time-series were rotated by the same amount, which simulates a typical patient behaviour (sudden head rotation followed by remaining in that position for a period of time) inside the scanner. The rotations were kept in the range $[0^\circ, 15^\circ]$ in the transverse direction (R_z).

We estimate perfusion parameters for DSC-MRI time-series using the perfusion mismatch analyser (PMA) tool [28]. PMA is free software used for CT and MR perfusion analysis, particularly for studying perfusion-diffusion mismatch. It calculates the basic maps like TTP, arrival time (AT) of contrast agent etc. Other quantitative maps like CBF, CBV and MTT are estimated using the basic maps via deconvolution [1]. Figure 2.3 shows various perfusion parameters maps obtained by using PMA tool on a typical DSC-MRI dataset.

We illustrate the effect of motion on two perfusion parameters: TTP and CBV. Patient motion causes misalignments of volumes in DSC-MRI time-series, which results in mixing of signal intensities of adjacent tissues in brain. This results in a partial volume effect (PVE). It has been shown that PVE affects the TTP maps [29]. The intermixing of signals from adjacent tissues affects the cerebral blood volume (CBV) parameter as well. To further analyse the effect of motion on these maps, we estimate perfusion parameters for a manually selected ROI for different degrees of motion. Figure 2.4 and Table 2.1 demonstrate the effect of patient motion on perfusion parameters TTP and cerebral blood volume (CBV) depending on the degree of motion. From these plots, it is seen that with an increase in the

[1] In signal processing, deconvolution is the process used to recover a signal. If h is the recorded signal, f is the signal to be recovered, but has been convolved with some other signal g, then the aim of deconvolution is to find the solution to the following convolution equation:

$$f * g = h$$

Different methods are used to estimate f, depending on whether g is known or unknown.

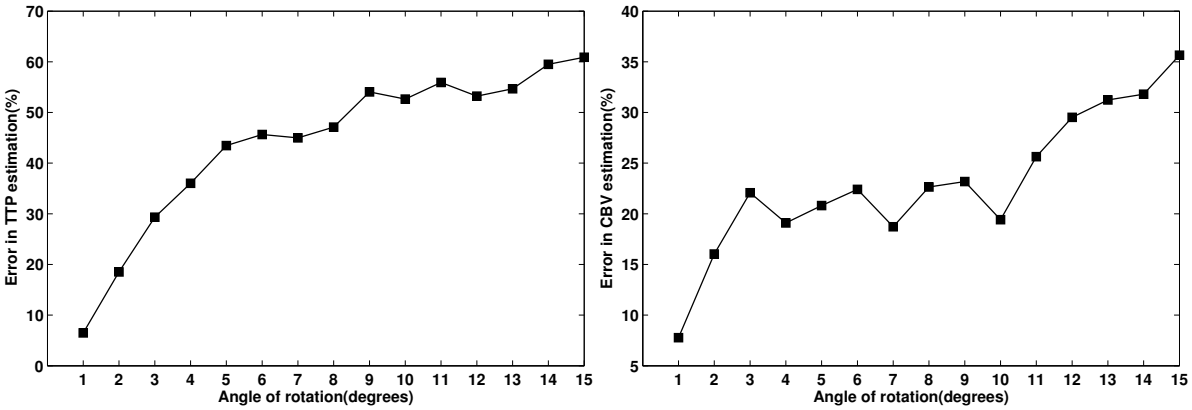

(a) TTP Plot **(b) CBV Plot**

Figure 2.4 Variation in estimation of parameters - TTP and CBV with different degrees of rotation.

degree of motion, the parameter estimation error increases with the error percentage exceeding 50% for TTP while it remains under 40% for CBV.

2.4 Summary

In this chapter, we introduced the concept of DSC-MRI which is used to study cerebral perfusion. We also discussed the different types of perfusion parameters associated with a perfusion (DSC/DCE MRI) studies. The objective of the chapter was to establish the effect of motion on perfusion parameters. The accuracy of estimation of perfusion parameters is based on a voxel-by-voxel tracking across time-points in the perfusion time-series. Patient motion during the scan results in intermixing of signals from adjacent regions like cerebro-spinal fluid (CSF) and white matter (WM) inside brain. This makes the estimation process inaccurate and can result in an erroneous diagnosis of the illness. The studies showed that the error in estimation of perfusion parameters can be as high as 40% for CBV and 50% for TTP for head rotation in the range $[0^\circ, 15^\circ]$ which is quite severe. Thus an accurate, reliable correction of the motion corrupted perfusion MRI data becomes necessary before it is further used for stroke diagnosis. The correction will give an accurate voxel-by-voxel analysis of different tissues inside brain and can prove helpful in treatment options. In the next chapter, we discuss the methods of motion correction in perfusion MRI used in the past. We also explain our proposed motion correction system that is able to overcome the shortcomings of existing methods.

Table 2.1 Clinical parameters - Time to peak (TTP) and CBV for a ROI for 16 datasets with different degrees of motion ($\mathbf{A}_\theta$ denotes parameter A estimated at angle of rotation θ°.)

Angle of rotation, $\mathbf{R_z}$ (in degrees)	**TTP (sec)**	**Difference from normal ($\mathbf{TTP_\theta - TTP_0}$)**	**CBV ($\mathbf{cm^3/100gm}$)**	**Difference from normal ($\mathbf{CBV_\theta - CBV_0}$)**
0	24.07	0	24.46	0
1	25.63	1.56	22.56	1.90
2	28.53	4.46	20.54	3.92
3	31.13	7.06	19.06	5.40
4	32.74	8.67	19.79	4.67
5	34.53	10.46	19.37	5.09
6	35.06	10.99	18.98	5.48
7	34.90	10.83	19.88	4.58
8	35.41	11.34	18.92	5.54
9	37.08	13.01	18.79	5.67
10	36.74	12.67	19.71	4.75
11	37.53	13.46	18.19	6.27
12	36.88	12.81	17.24	7.22
13	37.23	13.16	16.82	7.64
14	38.39	14.32	16.68	7.78
15	38.73	14.66	15.74	8.72

Chapter 3

Background, related work and proposed system

The volumes acquired in perfusion MRI time-series are spatially aligned with each other if the patient remains still for the entire acquisition period. Due to patient motion during acquisition of DSC-MRI data, the volumes get misaligned with respect to one another. Since, perfusion studies involve tracking a voxel across time-points, the misalignment of volumes results in losing track of a voxel with time. Formally, the voxel at location (x, y, z, t) in the first volume (V_1) would be located at location $(x', y', z', t+1)$ in V_2, at $(x'', y'', z'', t+2)$ in V_3 and so on. In a scenario where motion is absent, the voxel at (x, y, z, t) in V_1 can be tracked at location $(x, y, z, t+1)$ in V_2, at $(x, y, z, t+2)$ in V_3 and so on. There is a need to restore the motion corrupted perfusion time-series to a motion free series before it can be of any use in diagnosis. We can see that solving the problem of patient motion in DSC-MRI can be viewed as aligning the volumes in the time-series to one another. This is achieved by image registration. In this chapter, we explain the image registration technique that will help understand the motion correction process. Later, we discuss the methods used in the past to solve the motion corruption problem. We will find that majority of the methods use the image registration technique. Finally, we will propose our motion correction system that is able to overcome the shortcomings of the existing methods. We begin our discussion by introducing image registration as a method to align images.

3.1 Image Registration

Image registration is a process of geometrically aligning two images of the same object taken at different view-points, times or by different image acquisition techniques. It aligns the moving/sensed image to a reference image [61]. Basically, it finds the spatial transformation that maps the points in one image to its corresponding points in the other image. It is used in different areas like computer vision, medical imaging, remote sensing etc. In the medical domain, registration proves to be helpful in many applications such as abnormality detection, population studies etc. [24] [33] [13] [14] The image registration also helps to find the small changes that have occurred over time by removing the artefacts that can appear due to patient motion. Images of the same subject are acquired more than once and a single acquisition takes place over period of time. Figure 3.1 shows a framework for image

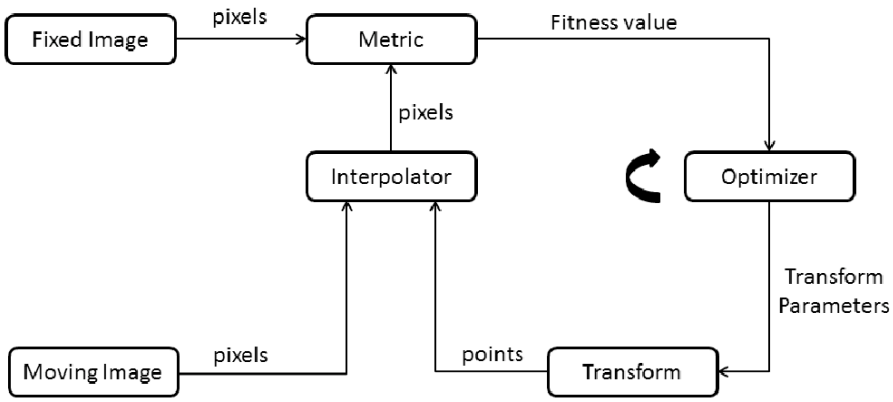

Figure 3.1 Block diagram of an image registration framework [59].

registration. Two input images, fixed (**F(x)**) and moving (**M(x)**) are provided as input. The aim of the registration is to find a spatial mapping to align the moving image to the fixed image. The transform (**T(p)**) is the transformation containing **p** parameters. We require a function that measures how well the images are registered. Similarity metrics such as squared difference and mutual information are popular.

Similarity

$\mathbf{S}(\mathbf{p}|\mathbf{F}, \mathbf{M}, \mathbf{T})$ is the similarity metric that determines the degree of alignment between the images. It provides the quantitative measure of how well **F(x)** and **M(x)** are aligned to each other. The metric can be thought of as a function of set of parameters for a given fixed image, moving image and type of transformation. Usually, the measure is computed by sampling points in the fixed image. For a given point **x** in **F(x)**, we find the corresponding moving point $\mathbf{x}' = \mathbf{T}(\mathbf{x}|\mathbf{p})$ using the transformation (T). The measure is then computed between these points. During registration, the moving image $\mathbf{M}(\mathbf{x})$, is iteratively transformed and the similarity metric is calculated. The choice of similarity metric depends on the application. Some metrics are applicable only when the images to be registered are from same modality, e.g. two MR images. In cases when the two images are from different modalities, e.g. a CT and MR image of same anatomy of a patient, other similarity metrics are needed. Two similarity measures used are:

Sum of squared difference (SSD)

The SSD measure was proposed by [22]. When the images to be registered are from the same modality, we use SSD metric. It is based on the assumption that corresponding points in images of same modalities must have similar intensities. Hence, this metric is commonly used in the field of computer vision. In the field medical imaging, it used when the images are of same modality, e.g. registration of

two T_1 MR images. The SSD measure is given by:

$$S(p|F, M, T) = \frac{1}{N} \sum_{i}^{N} [F(x_i) - M(T(x_i, p))]^2 \tag{3.1}$$

where, x_i is the i^{th} pixel of **F(x)**, N is the number of voxels in the overlapping region of two images. This measure is fast and can be used when both the images are of same modality. For different image modalities such as CT and MRI, the measure fails to work due to different intensities of same tissue in the two images.

Mutual Information (MI)

The concept of feature space as a measure to study alignment of images was proposed by [25]. Here, the feature space used was the 2D histogram of image intensities or other features constructed from the voxels where there is a correspondence or spatial overlap between the two images. Mutual information (MI) is a term used in the information theory which examines the statistical dependence of two random variables on one other, i.e. the amount of information one variable contains about the other. MI was proposed a measure for registration by [56][18] relating the entropies of two images with their joint entropy. The mutual information can be defined as:

$$I(F, M) = H(F) + H(M) - H(F, M) \tag{3.2}$$

where H(F) denotes the entropy of F, H(A) is the Shannon entropy of an image A. For a random variable X, the Shannon entropy is defined as:

$$H = -\sum_{i} p(x_i) log p(x_i) \tag{3.3}$$

where, $p(x_i)$ is the probability mass function of outcome x_i.

This measure is optimized by the optimizer over the search space defined by transformation parameters. In our work, we use limited memory Broyden-Fletcher-Goldfarb-Shanno method(l-BFGS) for optimization[23].

The transformations found in images can be of different types, rigid, non-rigid, affine etc. However, we limit our discussion to rigid transformations since we are studying MRI of brain that undergoes only rigid transformations due to patient motion. In the following section, we discuss rigid transformation model.

Rigid Transformation

The transformation T(p) is a defined by a set of parameters, p. A point x in fixed image F is mapped to point x' in moving image by[59]:

$$x' = T(x|p) \tag{3.4}$$

The image is mapped as:

$$T : \mathbb{R}^n \mapsto \mathbb{R}^m, F(T(x)) = M \tag{3.5}$$

where n and m are dimensions of fixed and moving image respectively. Rigid transformations are the geometric transformations that preserve all the distances, straightness of lines and angles between them. This kind of problem of estimating rigid transformations is called rigid registration. A rigid transformation consists of two components, translation and rotation. For 2D, this transformation is defined by three parameters $p = (t_x, t_y, \theta)$, where (t_x, t_y) are translation in 2D space and θ is the rotation. For a given point x in fixed image F, its corresponding homologous point X' can be found in moving image M as:

$$X' = \begin{bmatrix} x' \\ y' \\ z' \end{bmatrix} = \begin{bmatrix} cos\theta & -sin\theta & 0 \\ sin\theta & cos\theta & 0 \\ 0 & 0 & 1 \end{bmatrix} . \begin{bmatrix} x \\ y \\ z \end{bmatrix} + \begin{bmatrix} t_x \\ t_y \\ t_z \end{bmatrix} \tag{3.6}$$

hence, $\mathbf{x'} = \mathbf{T}(\mathbf{x}|\mathbf{p}) = \mathbf{T}(x, y|t_x, t_y, \theta)$. The challenge in registration lies with choosing the correct combination of optimization algorithm together with the similarity measure and transformation model that solve the required problem.

3.2 Related Work

Next, we discuss various methods used in past to solve the problem of motion correction in perfusion MRI. The standard approach to motion correction of 4D perfusion MRI data is via an alignment of all the motion corrupted volumes in the time-series to a chosen reference volume or the mean volume of the entire time-series data[26]. Due to the presence of contrast agent which causes non-uniform local variation in intensity of MR volumes, the traditional method of image registration cannot be used as such. Various developments in image registration techniques have attempted to solve the problem of dynamic contrast. To account for dynamic changes due to injected contrast agent, different motion correction methods have been used in the past. These can be broadly divided into following categories:

- Dynamic contrast independent image registration.
- Registration based on modelling dynamic change in contrast.

3.2.1 Dynamic contrast independent image registration

The methods used for motion correction in this category either ignore the change in contrast due to injected bolus or are invariant to dynamic change in contrast. [29] employs registration using six-parameter affine rigid body registration model with least squares minimization and fourth-degree B-spline interpolation for motion correction in DCE-MRI. The third volume in the time-series is used here as the reference volume. CBF maps estimated after motion correction were more accurate as compared to maps obtained for corrupted data. This method ignored the change in contrast due to bolus to achieve

a relatively simple method with lower processing time.

Multi-modal registration, methods that are independent of the variation in intensity between images have also been used. The different similarity measures associated with multi-modal registration technique account for the changes in contrast due to bolus. Similarity measures like mutual information [35] [57] and correlation ratio [43] are independent of change in contrast. However, the dynamic contrast due to injected bolus creates new features like pronounced edges of different tissue boundaries that cause these traditional techniques to fail.

[20] uses a motion correction model for global and local motion of kidney for DCE-MRI. This method uses normalized cross-correlation similarity measure which is invariant to changes in intensity. The perfusion curves of segmented kidneys derived before motion correction were found to be noisy. After applying motion correction, the curve displayed a typical behaviour of signal-time curve in DCE-MRI.

[54] uses a non-rigid B-spline image registration method that has been used for motion correction of 2D DCE-MRI solitary pulmonary nodules (SPNs). The similarity measure used here is mutual information. The contrast agent kinetic model estimated after correction helped in distinguishing the benign and malignant SPNs. This method requires human intervention: the region of interest is manually cropped and the reference image for registration is chosen manually.

[27] employs a feature based, group wise rigid registration in DCE-MRI images of diagnosis for breast cancer. The post-contrast images are registered to a group mean image, since there is very less contrast variation among these images. Subsequently, the group mean post-contrast image is registered to pre-contrast images. A contrast invariant image descriptor based on local steering kernel [48] is used for second registration.

[37] uses a progressive principal component registration method for registration of DCE-MRI images of liver. The principal components analysis (PCA) of the time-series data helps to avoid usage of costly physiological models used for modelling contrast agent intake. The method assumes that the signal containing enhancement will be found in the earlier eigen vectors of the PCA. With this assumption, the method iteratively generates motion free-synthetic time-series. The non-rigid registration method uses a cross-correlation based cost function.

[62] uses multi-modal image registration for motion correction. It is a two stage approach for motion correction in DCE-MRI of kidney. A 3D rigid registration is carried out in the first stage for removal of global motion due to movement of subject. The second stage consists of 3D non-rigid registration to remove artefacts due to local motion of the kidney. The similarity measure used here is mutual informa-

tion. The multi-modal registration technique proved invariant to the presence of injected contrast agent.

[60] propose a registration method based on a novel image similarity measure called robust estimation function. It is able to handle the intensity variation in DCE-MRI.

3.2.2 Registration based on modelling dynamic change in contrast

In this section, we discuss the methods proposed for motion correction that include the change in intensity due to injected bolus. Unlike methods discussed in the previous section, we will find that these methods are intensity dependent. These methods either model the intensity change or correct for intensity before the registration process is carried out.

[58] proposed a method that achieves simultaneous segmentation and registration of breast in DCE-MRI. A model for injected contrast agent is included here that accounts for dynamic variation in contrast. By estimating the relative signal change at every pixel in the image, the model can be fit to DCE-MRI time-series. The model then provides a mathematical model for signal-time variation in DCE-MRI. This provides a quantitative measurement of tissue characteristics in an image.

[12] proposed an iterative registration algorithm where synthetic data is generated from original data using pharmacokinetic modelling. The dynamic change in contrast is handled in the synthetic data which is then used in registration. Since the process is iterative in nature, the registered data is again used to generate synthetic data for the next iteration. The method has been used for tracking tumour motion. The tumour motion is limited to 3D translations only. The kinetic parameters can be estimated accurately after motion correction although the core of tumour region could not be estimated correctly. The iterative nature of the method and modelling the tracer kinetics makes it more costly. A similar approach has been used in [2].

[32] uses an intensity correction model to handle contrast variation in DCE-MRI. To further remove the variation in intensity, the registration of intensity corrected volumes is done using a floating scheme. First, two adjacent volumes, V_{n-1} and V_{n+1} in the time-series are registered to a chosen reference volume (V_n). Next, V_{n-2} is registered to V_{n-1} and V_{n+1} to V_{n+2}. This process is continued until the complete time-series is registered to V_n. The registration method failed to remove motion occurring in the volumes when the intensity correction was not used. With intensity correction prior to correction, bulk of the motion gets eliminated.

The two classes of methods discussed so far for motion correction in perfusion MRI either ignore the dynamic change in contrast, use multi-modal image registration methods or use a dynamic contrast change model to account for changes occurring in MR volumes due to presence of bolus. Ignoring the dynamic changes in intensity gives inaccurate results that can affect the diagnosis of the disease. Also,

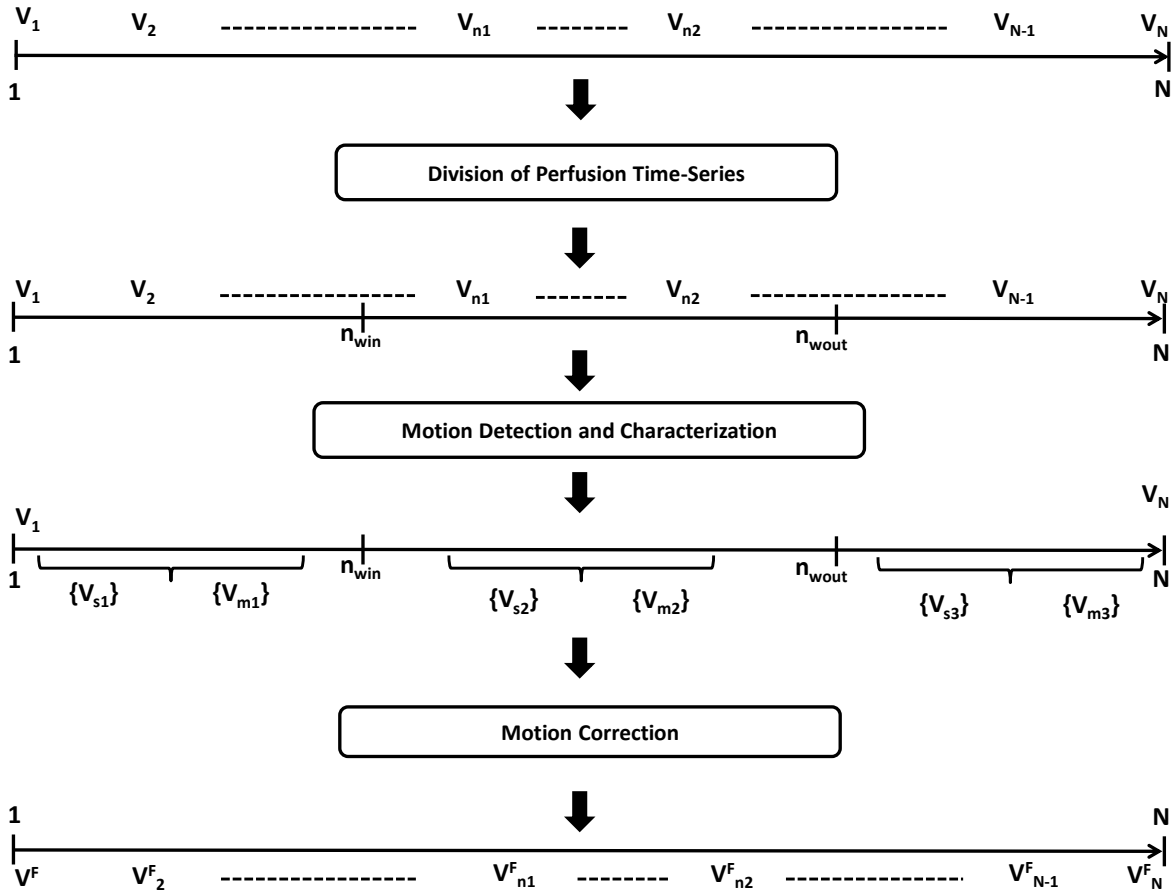

Figure 3.2 Framework for motion correction in perfusion weighted MRI. n_{win} and n_{wout} denote the wash-in and wash-out time-points of bolus respectively, V_i denote the volumes in the time-series, V_{si} and V_{mi} denote stationary (motion free) and moving (motion corrupted) volumes respectively, V_i^F denotes volume V_i aligned to global reference volume V^F.

in each of these methods, every volume in the time-series is aligned to a chosen reference volume using 3D registration. Hence, the methods discussed above are computationally intensive. Since time is of the essence in disease diagnosis, there is a need for a fast and efficient system of motion correction. In the following section, we propose such a system for motion correction in DSC-MRI time-series.

3.3 Our proposed system

The problem of motion corruption is a combination of a local and global phenomena. The presence of bolus in the region of interest within wash-in and wash-out time-points results in a local non-uniform contrast variation in the volumes acquired during that time-period. On the other hand, the patient motion during the complete duration of time-series acquisition results in a rigid transformation at the entire volume level. In general, motion correction has been found to be a time-limiting step ($\sim$90% of pro-

cessing time) in perfusion analysis [51]. Majority of the motion correction methods in perfusion MRI include aligning the volumes in the time-series to a reference volume via 3D registration. Since 3D registration is computationally intensive [49], it would be more efficient if only a subset of volumes need to be aligned instead of every volume in the entire time-series data. In general, if a time-series has N phases (or volumes), all the phases are not corrupted by motion. Hence, it is worthwhile to first detect the subset $\leq$ N volumes that is affected by motion and subsequently correct this subset. On the basis of this strategy, we propose a three stage system for motion correction in perfusion MRI as shown in Figure 3.2:

- Division of perfusion time-series
- Motion detection and characterization
- Motion correction

3.3.1 Division of perfusion time-series

This is the first stage of the three-stage motion correction system. In a perfusion time-series, two distinct time-points can be easily identified. These are the wash-in and the wash-out time-points. The volumes acquired prior to wash-in time-point and after wash-out time-point show no dynamic variation in image contrast due to absence of bolus. The volumes acquired between these two time-points are affected by bolus and thus depict slightly different behaviour than the rest. Keeping this in mind, we divide the time-series into three sets of volumes - set-1: pre-wash-in, set-2: transit and set-3: post-wash-out set. The perfusion time-series is divided by estimating the wash-in time-point (n_{win}) and wash-out time-point (n_{wout}) via curve fitting.

3.3.2 Motion detection and characterization

Once the time-series is divided into the three sets, we detect and characterize the motion present between volumes in the second stage. The motion detection is carried out in each of these sets independently. Since the volumes in set-2 in the time-series are affected by bolus, it is appropriate to choose a different method for motion detection in that set. Depending on the degree of motion occurring in a volume, we characterize the volumes into different motion categories - none, minimal, mild and severe motion.

3.3.3 Motion correction

This is the third and final stage of the system. Here, we align all the volumes in the time-series to a global reference volume in an intelligent manner. The motion correction in performed in two passes. In the first pass, the volumes in each of the sets are aligned to their respective reference volumes. After this pass, each volume in a set is aligned to its respective reference volume. In the second pass, we

align the reference volumes in each set to the global reference volume. In this way, we estimate the transformations required to align every volume in the time-series to global reference volume. Hence, we correct the volumes corrupted due to patient motion. The analysis of the system (discussed later) shows that it is fast and accurate thereby making the process of motion correction in perfusion time-series less costly.

3.4 Summary

In this chapter, we first introduced the concept of image registration which is the heart of algorithms used to correct for patient motion in perfusion MRI. Then, we discussed the methods used in the past to solve this problem. We classified these methods into two categories based on the manner in which they dealt with the dynamic change in contrast due to injected bolus. Finally, we proposed an efficient motion correction system built on a divide and conquer strategy that is able to overcome the shortcomings of existing methods. We present details of the proposed system in the forthcoming chapters. In the next chapter, we explain the first step of out motion correction system, i.e. division of perfusion time-series into different sets depending on the status of bolus.

Chapter 4

Division of perfusion time-series

The perfusion time-series is a union of three kinds of volumes: volumes acquired before the wash-in, volumes acquired between the wash-in and wash-out time-points and volumes acquired after the wash-out of contrast agent. The passage of bolus causes non-uniform contrast variation in the perfusion time-series. The problem in assessing the time-series as a single unit can create problems. Many motion detection or correction algorithms assume that the features in given two images remain the same. This assumption is violated in perfusion MRI. An example of this is the appearance of boundaries of affected regions in post-wash-in images as compared to pre-wash-in images. Hence, the accuracy of these algorithms maybe compromised if the complete time-series is analysed based on structure or information content. One can suggest including a dynamic contrast model in these algorithms [12], but in such cases it can prove to be costly. To overcome these problems, we propose a methodology wherein we divide the perfusion time-series into 3 disjoint sets depending on the status of bolus in brain. The division of time-series will help reduce the magnitude and cost of the problem of motion detection and correction as we will show further. In this chapter, we present a method to divide a perfusion time-series into above mentioned sets. We begin with discussion on the gamma-variate-function fitting on perfusion curves. This forms the basis of division of a perfusion time-series into disjoint sets.

4.1 Background: Gamma-variate-function fitting on perfusion curves

DSC-MRI consists of injecting a bolus of a paramagnetic contrast agent in a subject's blood stream and tracking it over time. This provides a signal-time curve of the region of interest (here brain). These signal-time curves can be converted to transverse relaxation rate change curves ($\Delta R_2(t)$ or $\Delta R_2^*(t)$). These relaxation rate changes depend directly on the contrast agent injected. Thus, with the help of these curves, we can estimate different perfusion parameters[7]. It is clear that an incorrect transverse relaxation curve will result in a wrong estimation of perfusion parameters which can prove to be fatal in terms of diagnosis[41]. The correct estimation of parameters can be achieved by modelling a suitable function to the passage of contrast agent in blood across time. The gamma-variate function [34] [16] models the transverse relaxation rate change-time curves, $\Delta R_2(t)$ or $\Delta R_2^*(t)$, with the first-pass(at

wash-in time) of the bolus. This function is given as:

$$\Delta R_2^*(t) = A(t - t_0)^{\alpha} e^{-(t-t_0)/\beta}, t > t_0 \tag{4.1}$$

where, $\Delta R_2^*(t)$ is the transverse relaxation rate of the magnetic field, t_0 is the wash-in time point of the bolus, and A, α and β are parameters that decide the shape of function. From Equation 2.2, the signal intensity S(t) is given by:

$$S(t) = S(t_0)(1 - e^{TR.\Delta R_1(t)}).e^{TE.\Delta R_2^*(t)}$$

Hence, an accurate fitting of ΔR_2^* curve gives an accurate change in signal intensity S(t).
The parameters A, α, β can be estimated using above equations [16]. Let us denote $\Delta R_2^*(t)$ by y(t). Hence, from Equation 4.1, we have:

$$y(t) = A(t - t_0)^{\alpha} e^{-(t-t_0)/\beta}, t > t_0 \tag{4.2}$$

Since, t_0 can be estimated easily, the above equation becomes:

$$y(t) = At^{\alpha} e^{-t/\beta} \tag{4.3}$$

When bolus peaks at time $t = t_{max}$, $\Delta R_2^*(t)$ (or y(t)) becomes maximum. Hence y'(t_{max}) will be 0. To estimate β, we take the first derivative of above equation:

$$y'(t_{max}) = At_{max}^{\alpha-1} e^{-t_{max}/\beta}(\alpha - \frac{t_{max}}{\beta})$$
$$\implies \beta = \frac{t_{max}}{\alpha}$$

Substituting β in Equation 4.3 at t=t_{max} gives:

$$y_{max} = y(t_{max}) = At_{max}^{\alpha} e^{-\frac{t_{max}}{t_{max}/\alpha}}$$
$$\implies A = y_{max}\left(\frac{e}{t_{max}}\right)^{\alpha}$$

Thus, Equation 4.2 can be written as:

$$y(t') = y_{max} t'^{\alpha} e^{\alpha(1-t')}$$

where, $t' = t/t_{max}$. Taking log, we get:

$$ln(y(t')) = ln(y_{max}) + \alpha(1 + lnt' - t')$$

The above equation can be solved for α, β and other parameters using least squares fitting. With this, we will be able to write a suitable gamma-function that fits the DSC-MRI data. In the following section, we use the above gamma-variate-function fitting method to divide the perfusion time-series volumes into disjoint sets.

4.2 Division of time-series into various sets

The given PWI time series of volumes $\{F_n; n = 1..N\}$ is divided into 3 distinct sets based on the status of the bolus in the brain. The method begins with the extraction of the mean intensity of each volume. This results in a curve $\mu_a(n)$. The gamma-variate function (GVF) in Equation 4.1 is next fit to $\mu_a(n)$ which results in GVF-fit-mean-intensity curve ($\mu_g(n)$). The wash-in (n_{win}) and wash-out (n_{wout}) time points are then determined using this curve as points of steep negative and positive transitions. It should be noted that estimating these points without the GVF fitting, while possible, will yield only rough estimates. These points help divide the given 4D dataset into three sets of volumes: Set 1 of pre-wash-in, Set 2 of transit and Set 3 of post-washout stage of the bolus passage. Figure 4.1 shows the central slices taken from volumes in each of these sets and also displays the mean-intensity profile for each set.

4.2.1 Pre-wash-in set

This set consists of the volumes acquired before the wash-in time-point. Since the bolus has not arrived by this time-point in brain, the set of volumes in this set are typical T_2^*-weighted MRI volumes. This set is referred to as Set 1. Figure 4.1 (a) show the central slices of a series of volumes taken from this set. The corresponding mean-intensity profile is shown in (b). As we can see from the figure, the mean-intensity of the volumes depicts a typical behaviour of T_2^*-weighted MRI time-series.

4.2.2 Transit set

The volumes in this set are acquired between the wash-in and wash-out time-points of bolus. As such, a localised non-uniform variation in contrast is observed in different regions of acquired volumes. This set is referred to as Set 2. Figure 4.1 (c) shows central slices extracted from volumes in this set. The variation of mean-intensity of these volumes shown in Figure 4.1 (d) describes the typical behaviour of T_2^* weighted DSC-MRI series.

4.2.3 Post-wash-out set

These volumes are acquired after the bolus has washed-out of the brain. Since the bolus does not affect these volumes, the contrast variation present in Set 2 volumes is not found here. This set is referred to as Set 3. Figure 4.1 (e) shows the central slices taken from volumes in this set. As we can see from the figure, the central slices are visibly similar. The mean-intensity profile shown in Figure 4.1 (f) describes this behaviour.

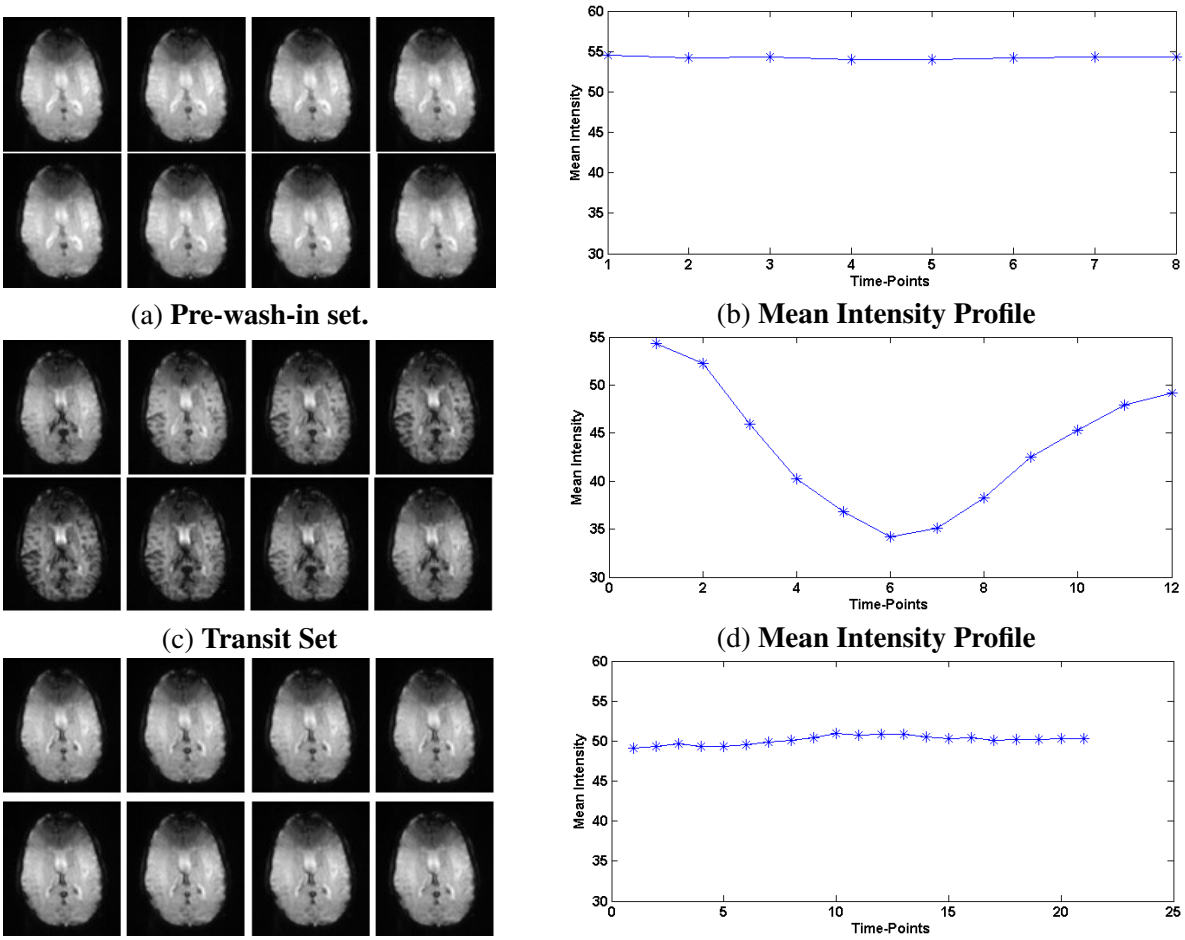

(a) **Pre-wash-in set.**

(b) **Mean Intensity Profile**

(c) **Transit Set**

(d) **Mean Intensity Profile**

(e) **Post-wash-out set**

(f) **Mean Intensity Profile**

Figure 4.1 Central slices taken from volumes from each of the sets in a DSC-MRI time-series

4.3 Results

Figure 4.2 shows an example of GVF-fitting on the mean-intensity curve of a perfusion series of 40 time-points. GVF-fitting here models the normal behaviour of first pass of contrast agent when passing through vasculature. The abrupt dip in GVF-fit-mean-intensity curve at time-point, n=10 represents the wash-in time-point of the contrast agent. GVF fitting is only applicable after the wash-in time-points, we can see from the figure that the behaviour of mean-intensity and GVF-fit-mean-intensity curves remain same before the wash-in time-point. However, the behaviour of the two curves differs in the transit region, where the GVF-fit-mean-intensity models the normal behaviour of contrast agent against the mean-intensity curve. Thus, the GVF-fit-mean-intensity curve provides a more accurate variation of intensity of regions that are affected by bolus across time-points. Once, the bolus has washed-out, which is represented by the flattening of the curve, here at time-point n=20, the behaviour of both the curves remains same owing to the fact that GVF-fitting models only the first-pass (wash-in) behaviour

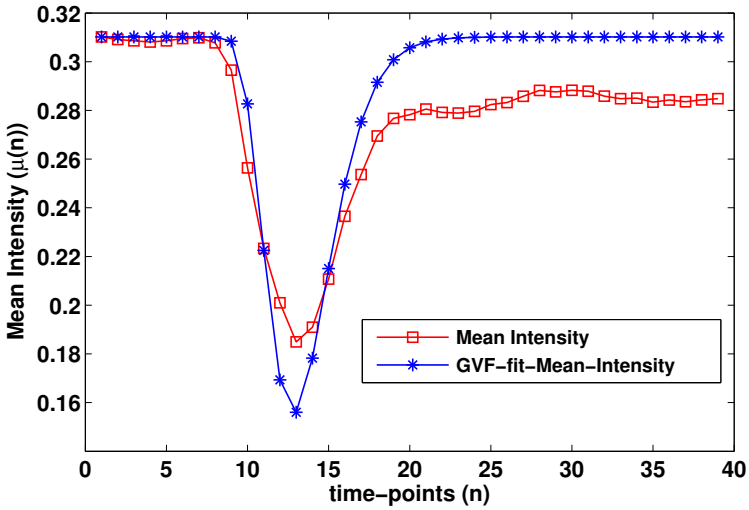

Figure 4.2 Gamma-variate-function fitting on the mean intensity curve of a DSC-MRI series.

of contrast agent. In the post-wash-out set, however, the GVF-fit-mean-intensity curve incorrectly lies above the mean-intensity curve. Hence GVF-fitting is not applicable in post-wash-out set.

4.4 Summary

In this chapter, we explained the first stage of the proposed motion correction, i.e. division of perfusion time-series into different sets, depending on the status of bolus in brain. The task was performed by fitting an appropriate gamma-variate-function (GVF) on the mean-intensity perfusion curve and identifying the time-points of steep negative and positive transitions in the GVF-fit-mean-intensity. Using these time-points, we divide the time-series into three distinct sets. This was the divide stage of a divide and conquer strategy. As we know that dividing a problem into sub-problems and solving them is easier than to take the problem in one go, we will see in the following chapters that this strategy forms the basis of proposed motion correction system. In the next chapter, we explain the second stage of motion correction system, i.e, detecting the presence of motion in volumes and quantifying them on the basis of the degree of motion to which these volumes get corrupted.

Chapter 5

Motion Detection and Characterization

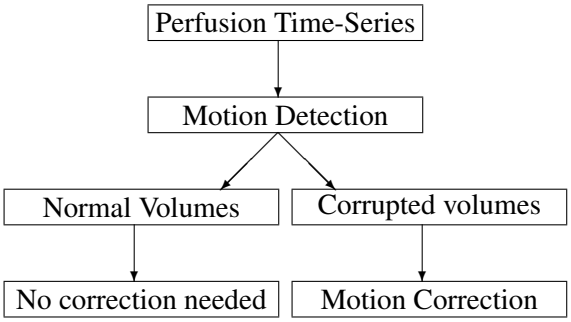

Figure 5.1 Utility of a motion detection stage in a motion correction framework. The introduction of a motion detection stage reduces the amount of work to be done.

Motion correction has been found to be a time-limiting step ($\sim$90% of processing time) in a PWI analysis pipeline [51]. Since 3D registration is computationally intensive [49] it would be more efficient if only a subset of volumes need to be aligned instead of every volume in the entire time-series data. In general, if a time-series has N phases (or volumes), all the phases are not corrupted by motion. Hence, it is worthwhile to first detect the subset $\leq$ N volumes that is affected by motion and subsequently correct this subset. An example of such a motion correction framework is shown in Figure 5.1. As we can see from the figure, such an approach reduces the amount of work to be done in motion correction by rejecting a subset of volumes from the time-series. The second stage in the proposed motion correction, i.e. the motion detection stage performs this task. In this chapter, we will discuss the motion detection method used to reject the stationary volumes in the time-series. The computational overhead for such a task cannot be more than the time consumed in aligning stationary volumes as it will defeat the purpose. We propose a fast motion detection technique to find the presence of motion in volumes in a DSC-MRI time-series. Based on the degree of motion present between volumes, we also assign the volumes into different motion categories.

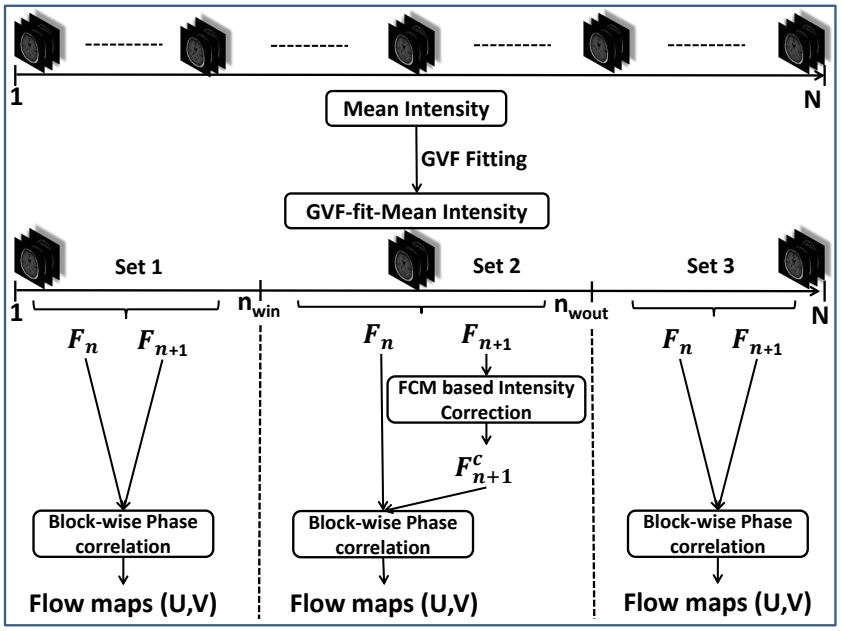

Figure 5.2 Motion Detection Scheme for a DSC-MRI time-series.

5.1 Motion detection framework

Figure 5.2 shows the block diagram for the proposed motion detection technique. In the first stage, the time-series is divided into 3 sets based on the status of bolus in brain, using GVF fitting. Next, motion is detected in each of these sets. The motion detection method for sets 1 and 3 (which correspond to pre-wash-in and post-wash-out) differs slightly from that of set 2 (between-wash-in-and-wash-out) due to the presence of bolus in set 2. In the following section, we explain the motion detection technique for PWI time-series in detail.

5.2 Motion Detection

Given a PWI time series, we aim to identify the volumes that are corrupted by motion. Since the scan time for a volume in DSC-MRI series is quite short ($\sim$ 2-3 seconds), it is fair to assume that there is no intra-volume subject motion present in the time-series. Consequently, every slice of a volume will be corrupted by the same degree of motion as the entire volume. Hence, we detect motion in the time-series between adjacent volumes using the central slices in every volume as shown in Figure 5.3. Our motion detection method is based on intensity correction and block-wise phase correlation. In the following section, we describe the traditional phase correlation technique.

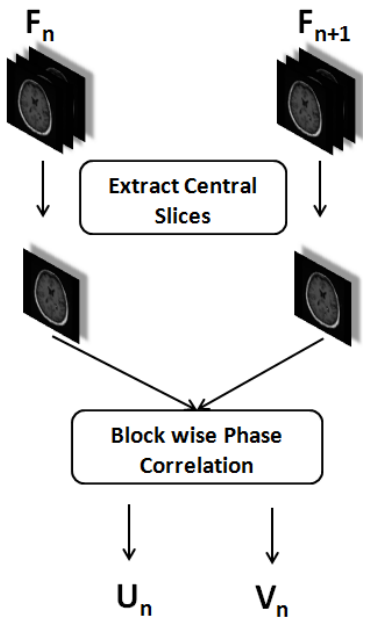

Figure 5.3 Motion Detection between two volumes in a time-series.

5.2.1 Background: Phase Correlation

Phase correlation is a technique that has been used for image alignment[10]. Phase correlation provides an estimation of rigid translational motion present between two images[31]. It is based on the Fourier shift theorem which states that a shift in the spatial domain of a signal corresponds to a linear phase shift in the Fourier domain.

Let $g_a(x) : \mathbb{R} \rightarrow \mathbb{R}$ and $g_b(x) : \mathbb{R} \rightarrow \mathbb{R}$ be two functions that are related as follows:

$$g_b(x) = g_a(x - x_0) \tag{5.1}$$

Then, according to the Fourier shift theorem,

$$\mathfrak{F}\{g_a(x - x_0)\} = G_a(\omega)e^{-j(\omega x_0)} \tag{5.2}$$

where $G_b(\omega)$ denotes $\mathfrak{F}\{g_b(x)\}$, the Fourier transform of $g_b(x)$. Hence,

$$G_b(\omega) = G_a(\omega)e^{-j(\omega x_0)} \tag{5.3}$$

The normalized cross-power spectrum ($S_{ab}(\omega)$) is

$$S_{ab}(\omega) = \frac{G_a G_b^*}{|G_a||G_b^*|} = e^{j(\omega x_0)} \tag{5.4}$$

The inverse Fourier transform of this function is an impulse which gives the shift.

$$\begin{aligned} r(x, y) &= \mathfrak{F}^{-1}\{S_{ab}(\omega)\} \\ &= \delta(x - x_0) \end{aligned} \tag{5.5}$$

Phase correlation thus enables determining the degree of translation between two images. A rotation between a pair of images can be visualized as a translation of pixels from location (x,y) in the first image to a new location (x-Δx, y-Δy) on the second image. Hence, the above approach can be used to determine the degree of motion. In the following section, we describe our approach to determine motion between adjacent volumes in DSC-MRI time-series data.

5.2.2 Proposed block-wise phase correlation

Given a pair of adjacent volumes (F_n, F_{n+1}) in a set, we consider only their central slices (I_n, I_{n+1}) and compute the motion field (U_n, V_n) between them. In the absence of any motion between the volumes, this field will be uniformly zero. The motion field is computed by considering a block of pixels $b(i,j)$ around every pixel at location (i,j) in the slice pair and performing a phase correlation. To handle the inter-slice intensity variation that is characteristic of DSC-MRI, the blocks are normalised first by shifting the mean pixel value of every block to zero. These normalised blocks are $\tilde{b}_n = b_n - \bar{b}_n$ where $\bar{b}$ denotes the mean pixel value in the block. Phase correlation is applied to the pair ($\tilde{b}_n(i,j)$, $\tilde{b}_{n+1}(i,j)$) and the desired flow vector $(u(i,j), v(i,j))$ is found from the locations of maxima of the cross power spectrum $S_{\tilde{b}_n \tilde{b}_{n+1}}$. The flow maps $U_n = u(i,j)$ and $V_n = v(i,j)$ describing the motion between I_n and I_{n+1} are given by:

$$(u, v) = argmax_{(i,j)\varepsilon b_{i,j}} \left(\mathfrak{F}^{-1} \left\{ S_{\tilde{b}_n \tilde{b}_{n+1}} \right\} \right) \tag{5.6}$$

where, $S_{\tilde{b}_n \tilde{b}_{n+1}} = \dfrac{\tilde{B}_n \tilde{B}^*_{n+1}}{|\tilde{B}_n||\tilde{B}^*_{n+1}|}$ and $\tilde{B} = \mathfrak{F}\{\tilde{b}\}$.

5.2.3 Motion detection for normal volumes

As the bolus is not present in sets 1 and 3, intensity correction is not required in these sets and motion can be detected in the volumes of these sets using block-wise phase correlation technique as explained above. In the following section, we explain the motion detection method for volumes that are affected due to bolus.

5.2.4 Motion detection for bolus affected volumes

In DSC-MRI, as the contrast agent passes through some regions in the brain, it results in signal attenuation only in those regions. This leads to a non-uniform intensity change within the volume. Applying motion detection to these volumes directly can result in an inaccurate estimation of motion present among these volumes. To overcome the problem of contrast variation, an intensity correction to the volumes in this set is needed prior to motion detection. Our intensity correction method is based on the fact that the bolus affects certain regions in brain and as such the contrast changes are found to be present in those regions only. Keeping this fact in mind, we devise a strategy to segment a given brain

volume into two regions: normal and bolus affected. The intensity correction is then applied to bolus affected regions and finally the mutually exclusive regions are combined to form an intensity corrected volume. This intensity corrected volume is then used for motion detection. In the following section, we explain the fuzzy c-means (FCM) clustering method used to segment a PWI volume.

5.2.4.1 FCM clustering based segmentation of volumes

Fuzzy c-means clustering is one of the methods in weighted clustering algorithms [39]. Fuzzy clustering is based on the fuzzy logic which is a form or probabilistic logic [8]. The reasoning behind fuzzy logic is that a particular phenomenon is approximate rather than exact or fixed. In fuzzy c-means clustering, every point in a given dataset has degree of belonging to a number of clusters instead of a single cluster [39].

The fuzzy c-means objective function for partitioning a set of points $\{x_n; n = 1..N\}$ into c clusters is given by [9]:

$$J = \sum_{i=1}^{c} \sum_{j=1}^{N} u_{ij}^{p} ||x_j - r_i||^2 \tag{5.7}$$

where, $\{r_m; m = 1..c\}$ are the representatives for each clusters and $[p_{ij}] = P$ is a partition matrix, $P \epsilon \Phi$, $\Phi \left\{ p_{ij} \epsilon [0\ 1] \middle| \sum_{i=1}^{c} p_{ij} = 1, \forall j\ and\ 0 \leq \sum_{j=1}^{N} p_{ij} \leq N\ \forall\ i \right\}$.

FCM clustering technique has been used for segmentation in images. A modified FCM clustering has been used for various purposes including bias field estimation and segmentation in MRI data [3], using spatial information for image segmentation [17], as a pre-processing step in brain MR images corrupt by RF-inhomogeneity [5]. We identify the bolus-affected regions using a fuzzy c-means (FCM) clustering method. This technique aids in segmenting a DSC-MRI volume F into normal (F_{normal}) and bolus affected (F_{bolus}) regions. After segmenting the volume into these two regions, we apply intensity correction as explained in the following section.

5.2.4.2 GVF-fitting based intensity correction

To account for changes in image intensity across time points, we use the previously explained GVF fitting on the mean-intensity perfusion curve ($\mu_g(n)$), to obtain the intensity change across time points. The intensity correction is then applied to only bolus affected regions. The intensity corrected volume is generated as follows. For convenience, the volume F at time point n is now denoted as $F(n)$:

$$\begin{aligned} F^{c}_{bolus}(n+1) &= F_{bolus}(n+1)\frac{\mu_g(n)}{\mu_g(n+1)} \\ F^{c}(n+1) &= F_{normal}(n+1) \cup F^{c}_{bolus}(n+1) \end{aligned} \tag{5.8}$$

where the superscript c denotes the corrected result. Figure 5.4 shows an example of intensity correction on a pair of slices with no motion between them. As compared to Figure 5.4(c), Figure 5.4(e) shows

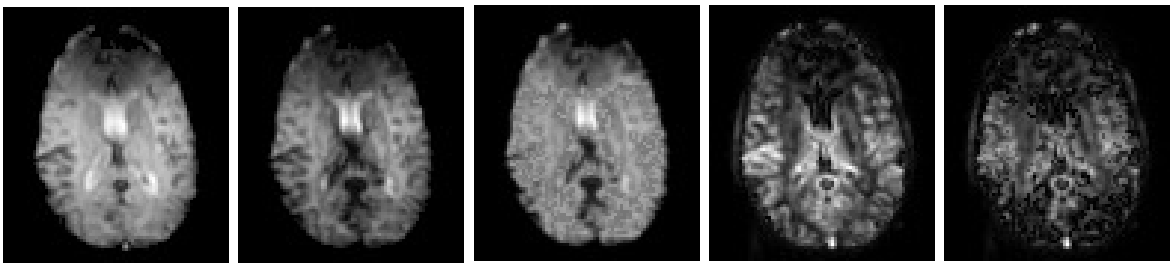

(a) $\mathbf{I_n}$ **(b) $\mathbf{I_m}$** **(d) $\mathbf{I_m^c}$** **(c) $|\mathbf{I_n} - \mathbf{I_m}|$** **(e)$|\mathbf{I_n} - \mathbf{I_m^c}|$**

Figure 5.4 Example of intensity correction for original (non-motion-corrupt) DSC-MRI data. Two central slices $\mathbf{I_n}$ and $\mathbf{I_m}$ extracted from volumes $\mathbf{F_n}$ and $\mathbf{F_m}$ are shown in (a) and (b) respectively. (c) is the intensity corrected image of (b). Notice that there is a reduction in absolute intensity difference in (e) as compared to (d). Ideally, the absolute difference in (e) should be zero.

a reduction in absolute difference in image intensity after intensity correction, which should ideally be zero. Nevertheless, the attenuation effect of bolus is minimised and this aids the correct estimation of motion between volumes.

5.2.4.3 Motion Detection

After intensity correction, we consider the central slices (I_n, I^c_{n+1}) of volumes (F_n, F^c_{n+1}) and carry out motion detection using block-wise phase correlation method as explained previously. The only difference here is that we use intensity corrected slices instead of raw DSC-MRI slices.

In our implementation, initially, a block size of 32×32 was used for motion detection in a slice of size 128×128. In an attempt to speed up computations, various downsampling factors of the central slice with a corresponding reduction in block size were also tested. The maximum downsampling factor achieved was 4 to obtain slice of size 32×32 and the block size was reduced to 8×8.

5.3 Motion Characterization

The flow maps U_n and V_n describe the orthogonal components of the flow field relating two representative slices (I_n and I_{n+1}) of the bolus-phase volumes of the time-series containing N volumes. In the absence of any motion, these flow maps, when viewed as images, will be uniformly smooth (all pixel values are equal). Presence of motion will introduce a disturbance in this map which can be characterized in terms of entropy in the each of these flow maps.

To ensure that noise related changes outside the brain tissue did not affect the motion metrics, a mask for the brain region was determined for each slice using a phase-field based segmentation of the bolus-time-slice [53]. A mask was generated individually for I_n and I_{n+1}. The union of the two masks was taken to ensure that entire span of motion in the two slices was captured by the mask. An entropy-based metric was used to quantify the degree of motion as follows: For a given time series $\{F_n; n = 1..N\}$,

Table 5.1 Different motion categories and their range of angles of rotation

Motion Category	Angle of Rotation (degrees)
no motion	0
minimal motion	[1, 5]
mild motion	[6, 10]
severe motion	[11, 15]

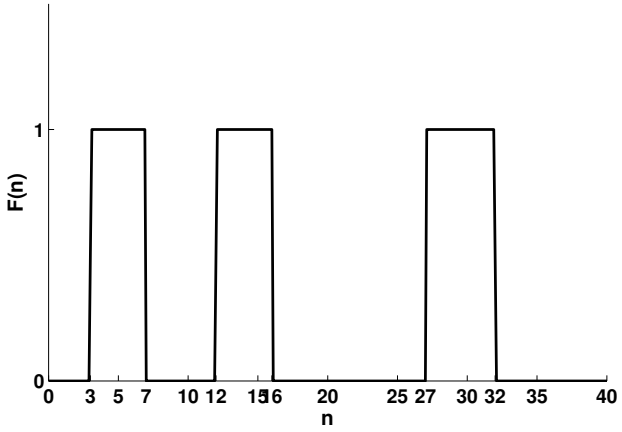

Figure 5.5 A plot showing the range of volumes(n) that are corrupted by motion in the time-series.

the flow fields (U_n, V_n) are computed first and the peak entropy H_{peak} of the flow fields is next found as

$$\begin{aligned} H_n &= H_{U_n} + H_{V_n} \\ H_{peak} &= max(H_n), 1 \leq n \leq N-1 \end{aligned} \tag{5.9}$$

where H_A denotes the Shannon entropy of A.

5.4 Experiments and Results

5.4.1 Dataset

A DSC-MRI dataset was acquired from a 1.5T GE MRI scanner with number of volumes = 40(1 second/phase), number of slices = 20, slice thickness = 5 mm, slice size = 128×128. All the computations were performed on Intel(R) Core(TM) i7-2600 CPU (3.40GHz) with 16GB RAM in MATLAB software.

In our experiments, simulated motion was applied to real perfusion data as real motion corrupted data was unavailable. For validating the proposed method, a set of experiments were performed. Known amount of 3D-rotation was added to the volumes to simulate actual patient motion during DSC-MRI

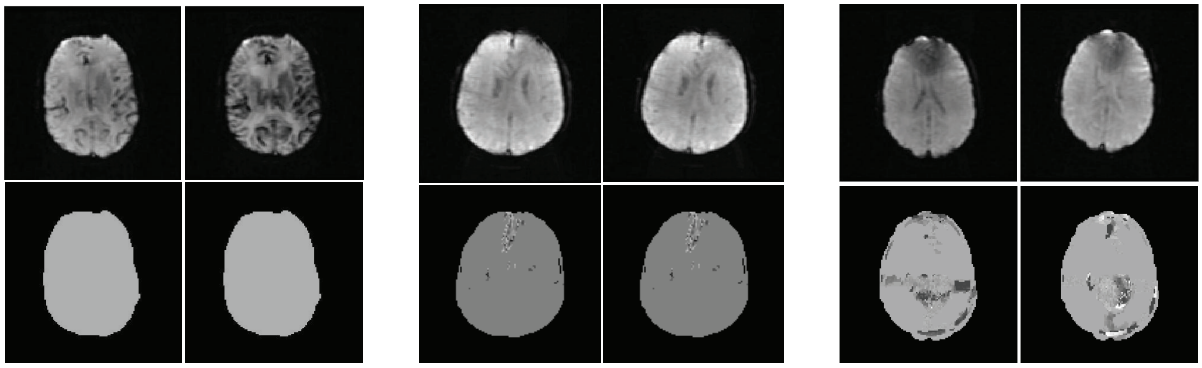

(a)No motion case **(b)Medium Motion case** **(c) Severe motion case**

Figure 5.6 Top row shows 3 sample slice pairs for different degrees of motion. Corresponding $\mathbf{U_n}$ and $\mathbf{V_n}$ flow maps are shown in the bottom row.

scan, in consultation with a neuro-radiologist. A number of consecutive volumes at repeated intervals in the time-series were rotated by the same amount, which simulates a typical patient behaviour (sudden head rotation followed by remaining in that position for a period of time) inside the scanner. For the DSC-MRI dataset of N=40 volumes, motion was added to $N_1 = 16$ volumes in m=3 blocks of contiguous volumes:{volumes at time-points in ranges [3, 7],[12, 16] and [27, 32] as shown in Figure 5.5}. The rotations were kept in the range $[0^\circ, 15^\circ]$ in the transverse direction (R_z) and in the range $[0^\circ, 10^\circ]$ in the coronal direction(R_x). For convenience in analysis, the motion corrupted volumes were categorized into different motion categories - none, minimal, medium and severe corrupted on the basis of angle of rotation. Table 5.1 shows different motion categories and their range of angles of rotation. This serves as ground truth for our experiments. All the results have been validated against this ground truth.

5.4.2 Results

We first present qualitative results (derived flow maps) for a pair of slices followed by quantitative results derived for the acquired dataset. Figure 5.6 demonstrates the phase-correlation based flow maps for different motion categories. As seen in Figure 5.6(a) (a no motion case), despite changes in the signal intensities, the flow maps are almost uniform, indicating that the proposed approach is mostly immune to bolus-contrast based signal changes. Further, as seen in Figure 5.6(b), the rotational motion creates disturbance in otherwise uniform flow maps even though there is no change in signal between two adjacent slices. The rotation of the bolus slice in Figure 5.6(c) (a severe motion case) creates a disturbance in the flow maps in areas which experience motion. Notice that despite changes in contrast (visible in areas around ventricles, Figure 5.6), the flow maps are uniform, indicating that the motion detection scheme is robust to contrast agent-related gradual signal changes.

Figure 5.7 demonstrates the variation of the net entropy metric (H_n) depending on the degree of motion between the slices for an entire time series (shown on the left). This information can be gleaned from the corresponding entropy profile per slice pair (shown on the right) which varies rapidly. It can be

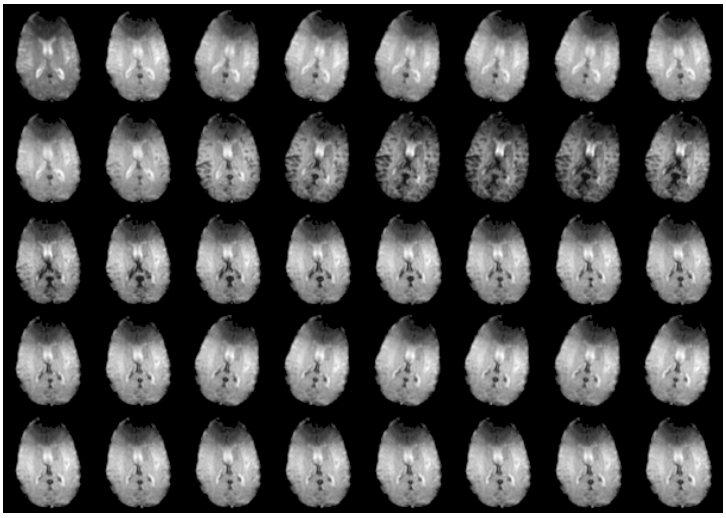

(a)DSC-MRI Time series

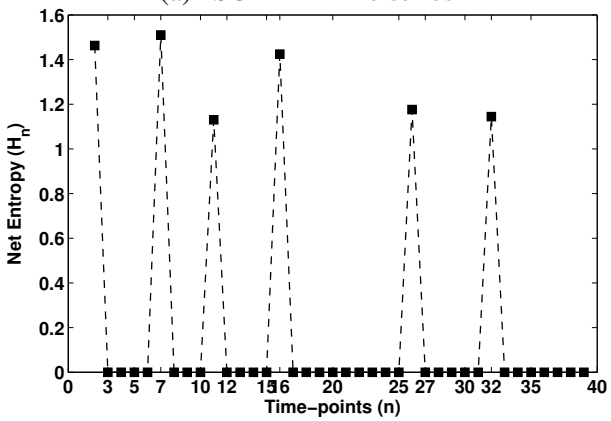

(b)Net-Entropy plot

Figure 5.7 Net-entropy($\mathbf{H_n}$) profile for a severe motion case. DSC perfusion data slices are shown across bolus-phases for n= 1 to 40 from left to right and top to bottom. First point in graph is the net entropy between slice 1 and slice 2 and so on.)

observed that for slice pairs between which there is minimal motion, the net entropy is zero, while for others, the entropy reflects the degree of motion. A more detailed picture of the entropy variation across bolus-phases for 16 different datasets is presented in Table 5.2. Here, the first column is the ground truth information. When the ground truth motion categories are compared with the peak entropy values, it is apparent that there is a mapping between them. Hence, it is possible to classify the data into different motion categories using the peak entropy (H_{peak}).

As indicated in Table 5.2 and Figure 5.8, the technique detects all categories of motion although for very small rotations (below 3°), it is difficult to distinguish it from no-motion case as the amount of entropy is mostly zero, resulting in poor sensitivity for this kind of motion. The sensitivity to detection is dependent on the image resolution and block size used for computations. In our experiments, the

sensitivity to minimal motion was found to be improve when the slice size was restored to the original size of 128×128. The sensitivity also increased when the block size was reduced from 32×32 to 16×16 for slice resolution 128×128. These were confirmed by visual inspection of the motion affected time-points. The increased sensitivity however, incurs an additional computational cost. Table 5.4 shows a detailed picture of time-taken for motion detection at different slice resolutions and block sizes. The average computation time per bolus-volume pair was 0.20 sec for a slice of size 32×32 (0.01 sec for down-sampling, 0.19 sec for deriving flow maps U_n and V_n) which increased to 3.48 sec for a slice of size 128×128. Thus, the overhead in computation is ∼17× for a 4× change in resolution and block size.

5.5 Evaluation

Since motion was added to volumes at time-points in intervals [3, 7],[12, 16] and [27, 32], the value of net-entropy (H_n) should be non-zero at the boundaries of these intervals. From Figure 5.7 (b), it can be seen that net-entropy (H_n) has a non-zero values at these boundaries. Hence, net-entropy metric can be used for motion detection.

Table 5.2 shows the entropy values for different degrees of motion. It can be seen that as the degree of motion increases, the entropy values increase. Peak entropy metric (H_{peak}) denotes the maximum net entropy value found in the time-series. Hence, H_{peak} can be used to categorize a time-series into different motion categories. Table 5.3 shows the upper and lower bounds of peak-entropies for different motion categories. Using these values, we can classify a time-series into one of the for motion categories. However, these values are not universal and are applicable to this dataset only.

Figure 5.9 illustrates the effect of intensity correction on motion detection using the net-entropy (H_n) plot for time series of 40 volumes with *mild* motion. To recall, the bolus phase is where the intensity correction is done. In the plot, the bolus stage is between $n = 9$ to 20. Two things can be observed from this plot: With no intensity correction, the net entropy value is i) higher in some of motion-affected volumes across the time series and ii) it is non-zero in adjacent stationary volumes only during the bolus phase. This is due to the fact traditional 2D block-wise phase correlation recognizes the variation in signal intensity as motion and gives a false positive result. On employing intensity correction, the net-entropy values for adjacent stationary volumes become zero as expected.

5.6 Summary

In this chapter, we discussed a method to detect motion between consecutive volumes using block based phase correlation in DSC-MRI perfusion data. The obtained flow maps describe the motion between slices. The net entropy in the flow maps was shown to help distinguish between varying degrees

Table 5.2 Entropy values for different motion categories for image resolution at 32x32 and block size at 8x8.

Motion Category (ground truth)	**Angle of rotation (in degrees)**	**Peak Entropy ($\mathbf{H_{peak}}$)**	**Total Entropy in U ($\mathbf{U_T} = \sum \mathbf{H_{U_n}}$)**	**Total Entropy in V ($\mathbf{V_T} = \sum \mathbf{H_{V_n}}$)**	**Total Entropy ($\mathbf{E_T} = \mathbf{U_T} + \mathbf{V_T}$)**
none	0	0.00	0.00	0.00	0.00
minimal	1	0.00	0.00	0.00	0.00
minimal	2	0.00	0.00	0.00	0.00
minimal	3	0.04	0.00	0.04	0.04
minimal	4	0.08	0.00	0.23	0.23
minimal	5	0.20	0.00	0.76	0.76
mild	6	0.25	0.00	1.29	1.29
mild	7	0.40	0.00	2.04	2.04
mild	8	0.52	0.00	2.67	2.67
mild	9	0.61	0.00	3.25	3.25
mild	10	0.75	0.08	3.78	3.86
severe	11	1.05	0.32	4.33	4.65
severe	12	1.15	0.48	5.14	5.62
severe	13	1.31	0.59	5.75	6.34
severe	14	1.37	0.85	6.21	7.06
severe	15	1.51	0.97	6.88	7.85

Table 5.3 Upper and lower bounds of peak entropy values for different motion categories.

Peak Entropy ($\mathbf{H_{peak}}$)	0	$0 < H_{peak} <= 0.25$	$0.25 < H_{peak} <= 1$	$H_{peak} > 1$
Motion Category	None	Minimal	Mild	Severe

of motion corrupted data. The main goal of this approach is to reduce the time for the motion correction process by removing the stationary volumes from the set of volumes to be registered and speed up the final (corrected) data acquisition process. The detection method can be made to be fast however the sensitivity to minimal motions may be compromised.

The emphasis here is on an effective motion detection technique which is immune to changes in signal intensity due to injected contrast. The utility of this work in retrospective motion analysis is to improve the time required for motion correction schemes with dynamic perfusion imaging data which currently accounts for as high as 90% of the data acquisition time.

Once motion detection has been performed, only a subset of volumes needs to be corrected for motion. In the next chapter, we discuss the third and final stage of our system that performs this task.

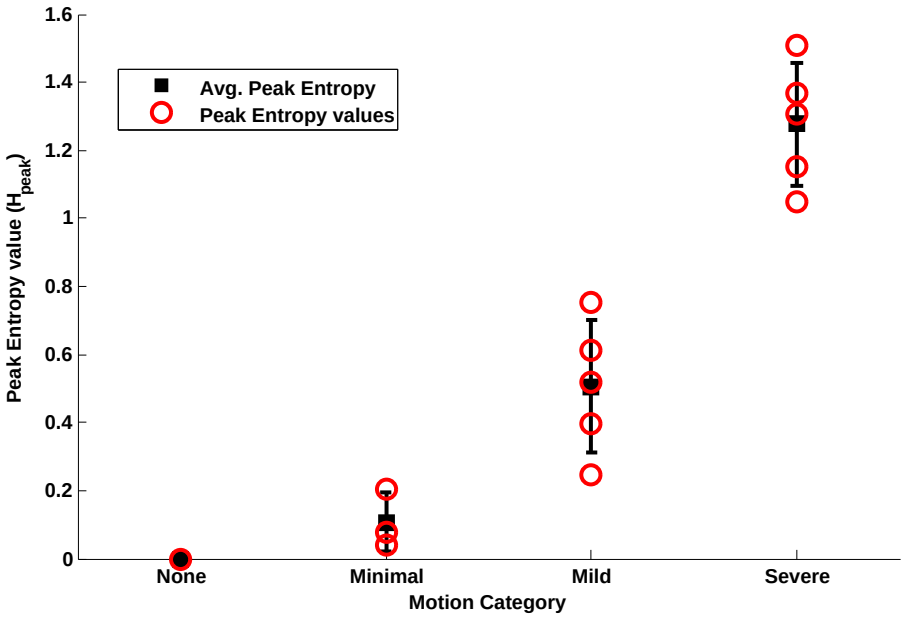

Figure 5.8 Peak Entropy metric for different motion categories on N = 16 datasets.

Table 5.4 Time analysis for motion detection at different slice resolutions and block sizes. Mean time per slice pair is the sum of time taken for downsampling and deriving $\mathbf{U_n}$ and $\mathbf{V_n}$ flow maps.

Slice Resolution	**Block Size**	**Mean Time per Slice Pair(sec)**	**Total Time(sec)**
128×128	32×32	0.00 + 3.48 = 3.48	132.21
128×128	16×16	0.00 + 3.99 = 3.99	151.69
128×128	8×8	0.00 + 4.34 = 4.34	164.84
64×64	16×16	0.01 + 0.77 = 0.78	29.71
64×64	8×8	0.01 + 0.97 = 0.98	37.38
32×32	8×8	0.01 + 0.19 = 0.20	**7.68**

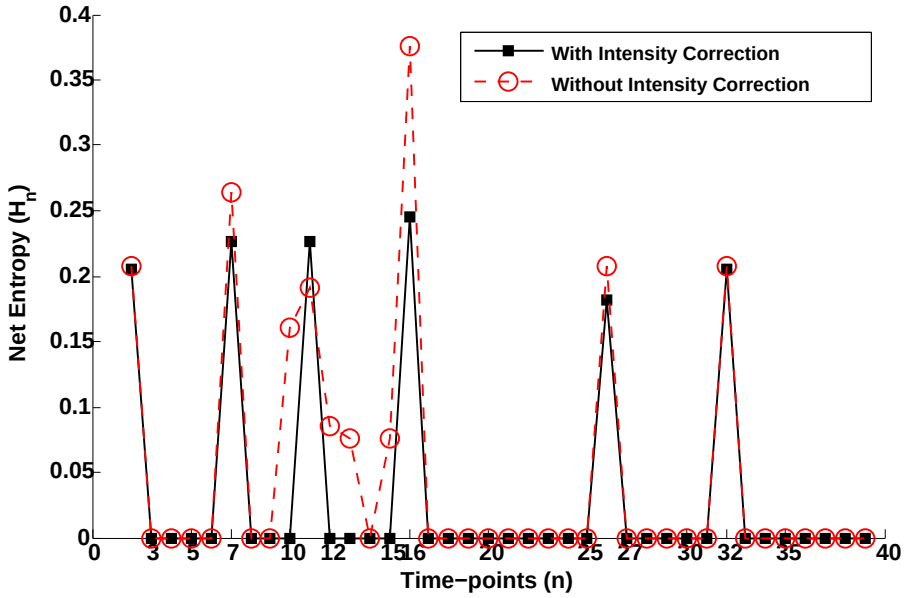

Figure 5.9 Net entropy($\mathbf{H_n}$) profile for motion detection with and without using intensity correction.

Chapter 6

Motion Correction

Motion correction of volumes in DSC-MRI time-series is the process of aligning the motion corrupted (moving) volumes in the time-series to a stationary (reference) volume. The core of such a task is 3D registration. In image registration, our aim is to estimate the transformation ($\mathbf{T}$) such that applying such a transformation on moving image will align it to reference image. If every image in a series of N images undergoes a different transformation, then registration will be required for each of them. Since image registration is computationally intensive, our aim should be to reduce the number of transformations to be estimated to bare minimum. In perfusion MRI time-series, the patient motion is not randomized. Thus, every volume does not undergo a different type of transformation due to patient motion. We take advantage of this fact and estimate only the required number of transformations thereby making the entire process efficient. In this chapter, we explain the last stage of proposed motion correction system where we align all the volumes in a DSC-MRI time-series to a global reference volume in an intelligent manner. We begin with the divide and conquer strategy, the heart of motion correction stage in the proposed system.

6.1 Divide and Conquer strategy for motion correction

Figure 6.1 shows the complete block diagram for the proposed divide and conquer strategy for motion correction in DSC-MRI. The first step in motion correction is to divide the given PWI time series into 3 distinct sets based on the status of the bolus in the brain. Next we detect the presence of motion in volumes in the time-series. Prior to this stage, the DSC-MRI time-series has already been divided into 3 sets of volumes: pre-wash-in, transit and post-wash-out stages using the gamma-variate-function fitting and we have detected the motion corrupted volumes in the time-series in the motion detection stage. Having performed both these tasks, we have divided the problem of motion correction of time-series into three similar sub-problems for each of the three sets. As in a divide and conquer strategy, we first solve the sub-problems and then use their result to solve the original problem. We employ a similar approach here.

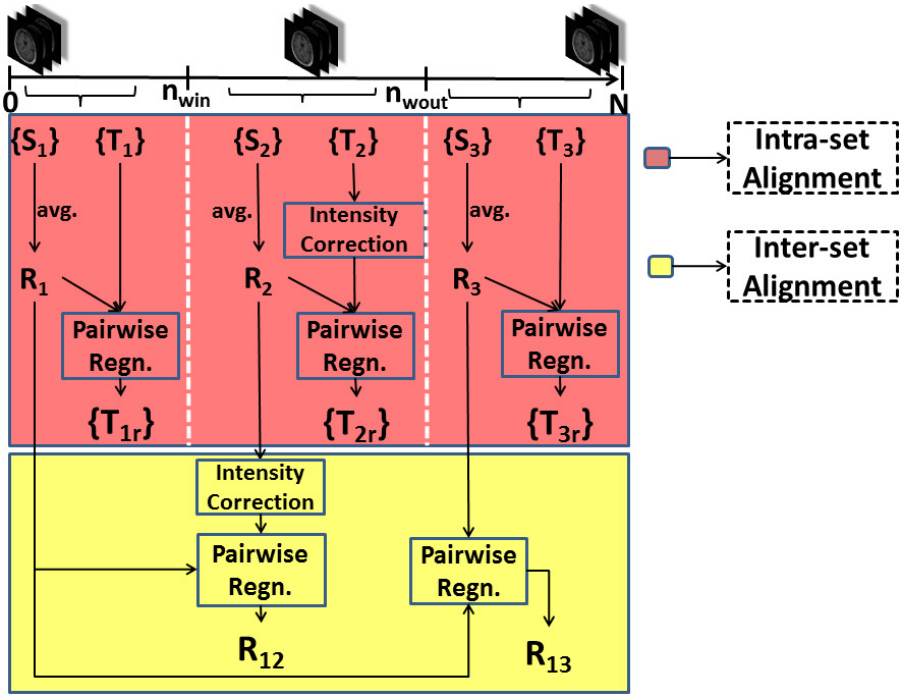

Figure 6.1 Block diagram for motion correction. $\{.\}$ denotes a set of volumes.

Motion correction is first carried out in each of these sets independently followed by a final registration step. A 2-pass process is designed for this purpose with the first pass aimed at intra-set alignment while the second pass aimed at inter-set alignment. In the intra-set alignment, we align the motion corrupted volumes in each of these sets to their respective reference volumes. The alignment process in each set is independent of each other. In the second pass, we align the reference volumes in each sets to a global reference volume. By a 2-pass registration scheme, individual transformations required to align every volume in the time-series to global reference volume can be estimated efficiently. The alignment of volumes in the time-series is done via 3D image registration. All pairwise alignments were done with sum of squared difference (SSD) based rigid registration using limited memory Broyden-Fletcher-Goldfarb-Shanno method(l-BFGS) for optimization[23]. This optimization technique has been shown to work well with large datasets[38]. In the following section, we explain the first pass of the proposed 2-pass alignment scheme.

6.2 Intra-set Alignment of volumes

The intra-set motion correction is the first pass of a 2-pass motion correction scheme. In the first pass, the motion corrupted (moving) volumes in each of the three sets are aligned to their respective reference(fixed) volumes via registration. These reference volumes are created using the contiguous stationary volumes found during the motion detection stage. The process of alignment of volumes in set

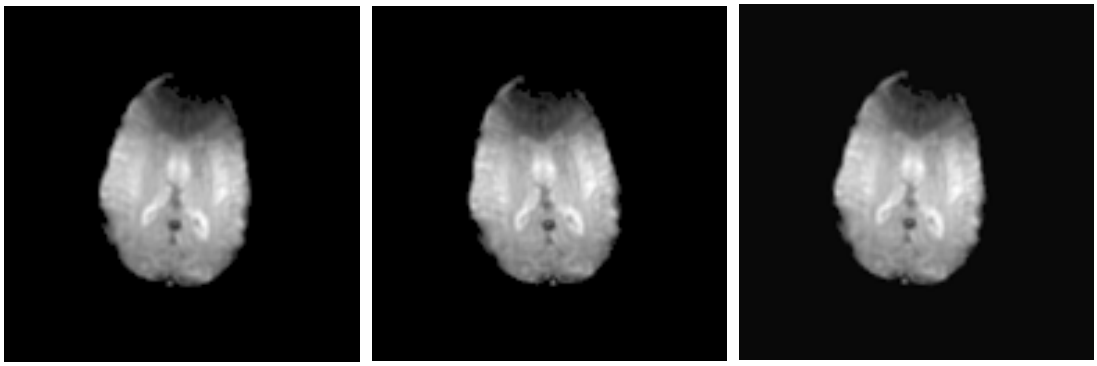

(b) $\mathbf{Reference - R_1}$ (a) $\mathbf{Moving - T_1(i)}$ (c) $\mathbf{Registered - T_{1_r}(i)}$

Figure 6.2 Alignment of a motion corrupted volume in set-1 to R_1.

2(transit stage) differs from the process used for set 1(pre-wash-in stage) and set 3(post-wash-out stage) due to the presence of bolus in transit stage. First, we explain the process of creation of these reference volumes.

6.2.1 Creation of reference volumes

In the construction of reference volume for registration, the fact that the subject motion (during acquisition) is transient in nature, i.e. stationary for a set of contiguous time-points followed by an irregular motion for short period of time can be exploited. In the motion detection stage, we detect motion between adjacent volumes in the time-series. Using entropy metric, we were able to categorize volumes into different motion categories. The entropy value is zero for adjacent pairs where there is no motion. This helps to identify the contiguous set of volumes for which the subject has remained stationary. Hence, the reference volume R_m for each stage of the bolus (before, during and after the passage) is constructed as:

$$R_m = \frac{\sum_{n=n_1}^{n_2} S_m(n)}{(n_2 - n_1 + 1)}, \quad m\epsilon\{1, 2, 3\} \tag{6.1}$$

where, $S_m(n)$ is a stationary volume,$(n_2 - n_1)$ is the longest time interval of contiguous stationary volumes in the m^{th} set. After creation of reference volumes, we align the motion corrupted volumes via registration. In the following section, we explain the alignment of set-1 and set-3 volumes to their reference volumes.

6.2.2 Alignment of volumes in pre-wash-in and posh-wash-out stage

The bolus does not affect the volumes acquired in these two stages, hence the volumes in these two stages are aligned to their respective reference volumes created by Equation 6.1 by 3D registration. Figure 6.2 and Figure A.1 show the result of intra-set alignment of corrupted volumes taken from each

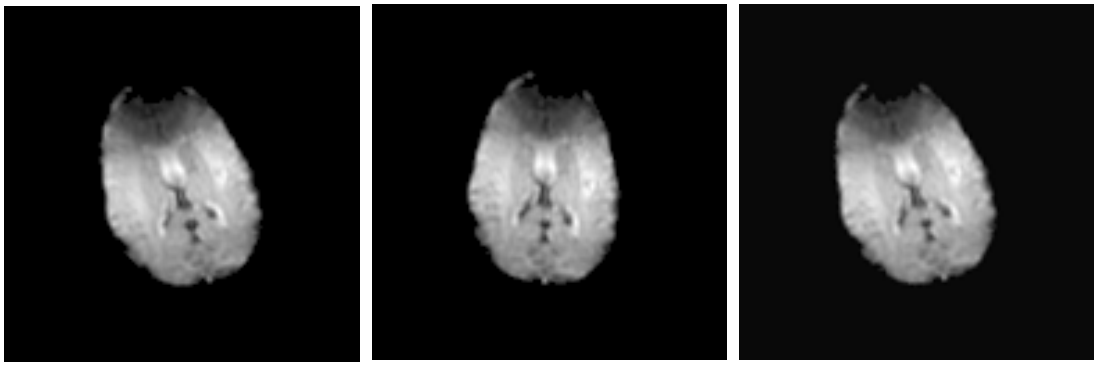

(a) $\mathbf{R_3}$ (b) $\mathbf{T_3(k)}$ (c) $\mathbf{T_{3_r}(k)}$

Figure 6.3 Alignment of a motion corrupted volume in set-3 to R_3.

of these two sets. The intra-set alignment of the volumes acquired during the transit stage is explained in the following section.

6.2.3 Alignment of volumes in transit stage

The presence of bolus in transit stage creates difficulties in alignment of the motion corrupted volumes. The localised non-uniform change in intensity due to bolus causes the intensity based registration method to fail. To overcome this problem, first we apply an intensity correction to the volumes in this set. The intensity correction volumes are aligned to set-2 reference volume subsequently. In the following section, we explain the intensity correction method.

6.2.3.1 Intensity correction of volumes

In DSC-MRI, there is a signal loss or decrease in the image intensity, only in regions where the bolus is present. This leads to a non-uniform intensity change within the volume. We identify the bolus-affected regions using a Fuzzy c-means clustering method. This aids in segmenting the moving volume (F) into normal (F_{normal}) and bolus affected (F_{bolus}) regions. To account for changes in image intensity across time points, we use the gamma-variate function fitting on the mean-intensity perfusion curve ($\mu_g(n)$), to obtain the intensity change across time points. The intensity correction is then applied to only bolus affected regions. The intensity corrected moving volume $F^c(n)$ is generated by:

$$\begin{aligned} F^c_{bolus}(n) &= F_{bolus}(n)\frac{\mu_g(n_{R_2})}{\mu_g(n)} \\ F^c(n) &= F_{normal}(n) \cup F^c_{bolus}(n) \end{aligned} \tag{6.2}$$

where, n_{R_2} is the centre of time-points used for constructing reference volume R_2. This results in a reduction of the contribution of bolus in intensity difference and makes the similarity measure in registration more accurate. The alignment of volumes in set-2 to their reference volume is explained in the following section.

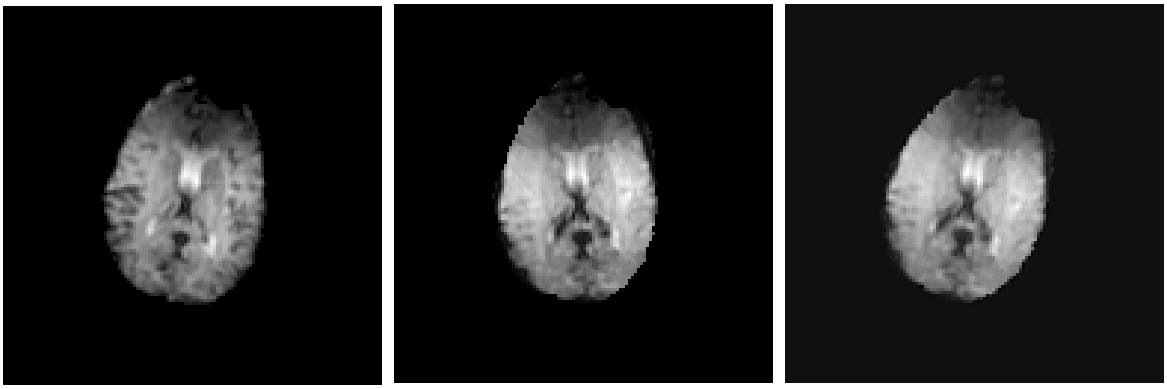

(a) $\mathbf{R_2}$ (b) $\mathbf{T_2(k)}$ (c) $\mathbf{T_{2_r}(j)}$

Figure 6.4 Alignment of a motion corrupted volume in set-2 to R_2.

6.2.3.2 3D registration of intensity corrected volumes

The aim of the intensity correction was to remove the effect of change in contrast due to bolus. Hence, once the volumes in the transit stage are corrected for intensity with respect to their reference volume, the intensity based registration method can be used for alignment of motion corrupted volumes. Thus, the moving volumes in set-2 are aligned to the reference volume R_2 by 3D registration method. Figure 6.4 shows the result of alignment of a moving volume in set-2 to reference volume R_2.

At the end of intra-set alignment, we have required transformations to align the moving volumes in each set to their reference volumes. Let Y_{1i}, Y_{2j} and Y_{3k} be the transformations relating (R_1,$T_1(i)$), (R_2,$T_2(j)$) and (R_3,$T_3(k)$) respectively where $T_m(n)$ denotes n^{th} moving volume in m^{th} set. These can be used to align the corrupted volumes in Sets 2 and 3 to R_1 as follows:

$$\begin{aligned} T_1(i) &\xrightarrow{Y_{1i}} T_{1_r}(i); \quad i\epsilon[1, n_1] \\ T_2(j) &\xrightarrow{Y_{2i}} T_{2_r}(j); \quad j\epsilon[1, n_2] \\ T_3(j) &\xrightarrow{Y_{3i}} T_{3_r}(k); \quad k\epsilon[1, n_3] \end{aligned} \tag{6.3}$$

where, n_m denote the number of corrupted volumes in m^{th} set. After the intra-set alignment, we align the reference volumes in each of the sets to a global reference volume. This is done in the second pass, i.e. the inter-set alignment step. In the following section, we explain the inter-set alignment method.

6.3 Inter-set Alignment

The reference volume created for the first set (R_1) is taken to be the global fixed reference (R_{final})for the entire DSC-MRI time-series. In the second pass of alignment, i.e. the inter-set alignment, we align

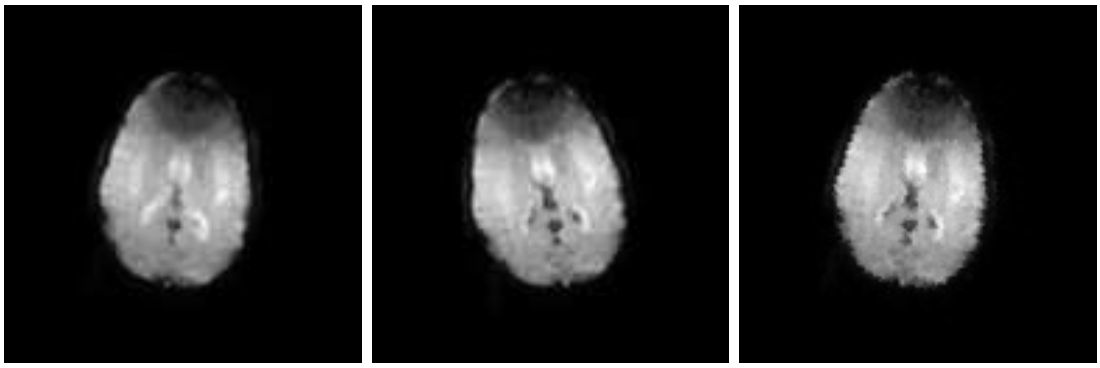

(a) $\mathbf{R_{final}}$ (b) $\mathbf{R_3}$ (c) $\mathbf{R_{f3}}$

Figure 6.5 Alignment of reference volume R_3 to R_{final}.

the reference volumes of transit (R_2) and post-wash-out (R_3) stages to the global reference volume (R_{final}). In the following section, we explain the registration of R_3 to R_{final}.

6.3.1 Alignment of reference volume $\mathbf{R_3}$ to $\mathbf{R_{final}}$

Since the bolus has not affected the volumes in these time-points, hence the reference volumes created in these stages are not affected by bolus too. We align the reference volume R_3 to global reference volume R_{final} via 3D registration method. Figure 6.5 shows the result of alignment of R_3 to R_{final}. In the following section, we explain the inter-set alignment of R_2 and R_{final}.

6.3.2 Alignment of reference volume $\mathbf{R_2}$ to $\mathbf{R_{final}}$

The alignment of reference volume R_2 to R_{final} is done in two steps. Since the bolus affects volumes in set-2, the reference volume R_2 is also affected by bolus. Thus, first we apply an intensity correction on R_2 and then the intensity corrected reference volume is aligned to global reference volume R_{final}. In the following section, we explain the intensity correction method.

6.3.2.1 Intensity correction for $\mathbf{R_2}$

Since the bolus is present in the volumes in second set or the transit set, the reference volume R_2 needs to be corrected for intensity before it is aligned to final reference volume R_1. We identify the bolus-affected regions using a Fuzzy c-means clustering method as explained previously. This aids in segmenting the reference volume (R_2) into normal ($R_{2_{normal}}$) and bolus affected ($R_{2_{bolus}}$) regions. To account for changes in image intensity across time points, we use the gamma-variate function fitting on the mean-intensity perfusion curve ($\mu_g(n)$), to obtain the intensity change across time points. The intensity correction is then applied to only bolus affected regions. The intensity corrected reference

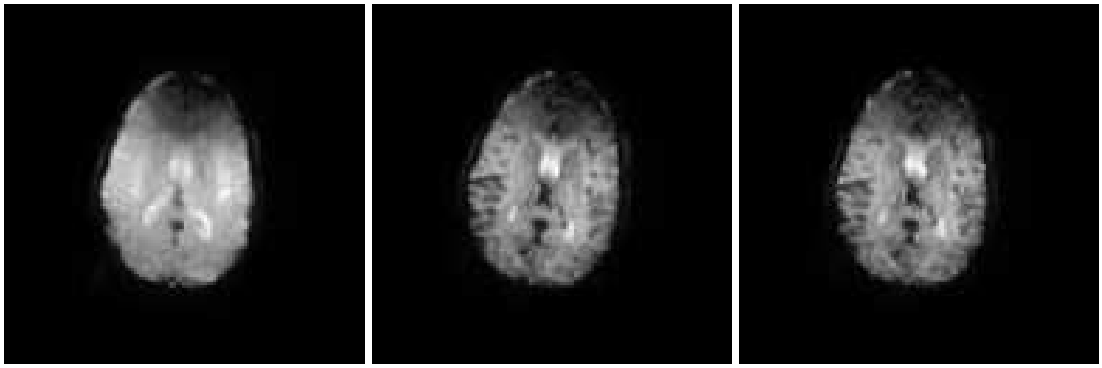

(a) $\mathbf{R_{final}}$ (b) $\mathbf{R_2}$ (c) $\mathbf{R_{f2}}$

Figure 6.6 Alignment of reference volume R_2 to R_{final}.

volume R_2^c is generated by:

$$\begin{aligned} R^c_{2_{bolus}} &= R_{2_{bolus}} \frac{\mu_a(n_{R_1})}{\mu_g(n_{R_2})} \\ R^c_2 &= R_{2_{normal}} \cup R^c_{2_{bolus}} \end{aligned} \tag{6.4}$$

where n_{R_1} and n_{R_2} are the centre of time-points used for constructing reference volumes R_1 and R_2. This results in a reduction of the contribution of bolus in intensity difference and makes the distance measure in registration more accurate. Please note that in the above equation, we have used $\mu_a(n_{R_1})$ instead of $\mu_g(n_{R_1})$ for intensity correction of R_2 with respect to R_1. Since GVF fitting is applicable only for volumes that are acquired after bolus has washed in, the usage GVF-fit-mean-intensity ($\mu_g(n_{R_1})$) for intensity correction would be incorrect here.
Once the reference volume R_2 has been corrected for intensity, it is aligned to the global reference volume R_{final} as explained in the next section.

6.3.2.2 3D registration of intensity corrected reference volume $\mathbf{R_2^c}$ to $\mathbf{R_{final}}$

After the reference volume R_2 has been intensity corrected to create R_2^c with respect to final reference volume R_1, the intensity based registration method can be applied to align the R_2^c to R_{final}. Thus, we align R_2^c to R_{final} using 3D registration method. The estimated transformation relating R_2^c to R_{final} is used to align R_2 to R_{final}. Figure 6.6 shows the result of alignment of R_2 to R_{final}. Despite the changes in contrast, R_2 is correctly registered to R_{final} to produce the registered output (R_{f2}).
The aim of motion correction is to align all the volumes in the time-series to a reference volume. After the completion of inter-set alignment, we align the entire time-series to reference volume R_{final} as explained in the next section.

6.4 Alignment of the entire DSC-MRI time-series

At the end of inter-class alignment we have all required transformations to align the complete time series. Let X_{f2} and X_{f3} be the transformations relating (R_{final},R_2) and (R_{final},R_3) respectively. These can be used to align the corrupted volumes in Sets 2 and 3 to R_{final} as follows:

$$\begin{aligned} T_2(j) \xrightarrow{Y_{2i}} T_{2_r}(j) \xrightarrow{X_{f2}} T_{f2_r}(j); \quad j\epsilon[1, n_2] \\ T_3(j) \xrightarrow{Y_{3i}} T_{3_r}(k) \xrightarrow{X_{f3}} T_{f3_r}(j); \quad k\epsilon[1, n_3] \end{aligned} \tag{6.5}$$

6.5 Experiments and Results

6.5.1 Dataset

A DSC-MRI dataset was acquired from a 1.5T GE MRI scanner with number of volumes = 40(1s/phase), number of slices = 20, slice thickness = 5 mm, matrix size = 128×128. For validating the proposed method, a set of experiments were performed. All the computations were performed on 64-bit Intel(R) Core(TM)2 Duo processors(2.20 GHz) with 2GB RAM and MATLAB v7.12.0.

In our experiments, known amount of 3D rotation were added in the volumes to simulate patient motion during DSC-MRI. Transient nature of motion was reflected by adding motion to volumes at a random interval of time-points. The rotation angles were generated randomly in the range [-20° 20°] in transverse direction(R_z) and [0° 10°] in coronal direction(R_x). The randomness in generation of angles captures the worst case scenario of motion where the subject is highly agitated. Translation motion inside the scanner is found absent in most of the cases. These ranges were chosen on the advice of a neuroradiologist as depicting typical patient motion.

6.5.2 Results

We first present qualitative results of registration with our approach. Figure 6.7 shows the entire aligned time-series with our approach. Despite changes in the contrast in bolus phases, the entire perfusion series gets aligned to global reference volume (R_{final}). The alignment was quantitatively assessed using the dice coefficient of segmented brain masks. The dice coefficient (DC) measures the degree of overlap between two regions. For two sets A and B, the measure is given by:

$$DC = 2\frac{A \cap B}{A \cup B} \tag{6.6}$$

A DC value of 1 indicates perfect alignment. With R_1 as the reference volume, the DC values are presented in Table 6.1 for all the registered volumes in the time-series. After registration, the degree of overlap between the volumes increases which is verified by the DC values before and after registration.

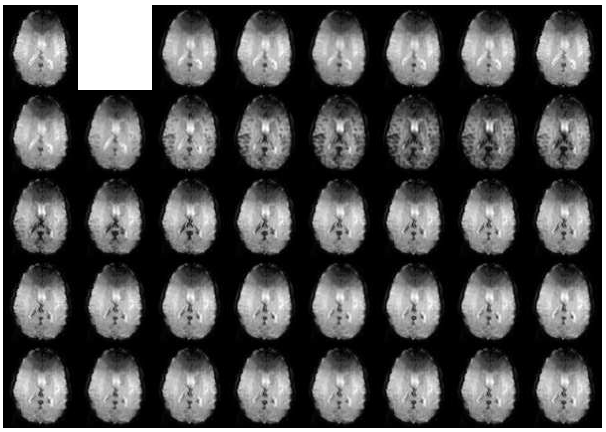

Figure 6.7 Central slices of volumes after alignment of entire-time series. DSC perfusion data slices are shown from left to right and top to bottom. First slice is taken from the global reference volume (R_{final}).

Table 6.1 Dice Coefficient(DC) values before and after motion correction

Rotation in R_z(degrees)	Rotation in R_x(degrees)	DC before Registration	DC after Registration
[0 10]	[-10 10]	0.88	**0.93**
[0 10]	[-15 15]	0.86	**0.92**
[0 10]	[-20 20]	0.87	**0.93**

A second type of evaluation was done to study the effect of registration on mean-intensity of a manually selected volume of interest (VOI) before and after registration. The results are shown in Figure 6.8. Prior to registration, subject motion causes a shift in VOI and intensity-time curve does not depict a typical behaviour of DSC-MRI. After registration, the VOI remains stationary across time-points and a typical DSC-MRI intensity-time curve is obtained. A detailed picture of mean-intensity curves before and after motion correction for different degrees of motion is given in appendix.

6.6 Evaluation

The performance of our approach was also compared with traditional registration techniques reported in literature where the whole time-series is registered to a mean volume [26]. The evaluation metric chosen for this purpose was the RMS difference of the residual difference (e_{rms})[44] defined as:

$$e_{rms} = \sqrt{\frac{1}{N}\sum_{\mathbf{x}\epsilon\Omega}(U_a^{-1}(\mathbf{x}) - U_o(\mathbf{x}))^2}; \quad \mathbf{x} = [x, y, z]^T \tag{6.7}$$

where, U_a is the applied transformation and U_o is the obtained transformation, N is the number of voxels in object Ω. Table 6.2 provides a detailed comparison of performance of our approach and an MI based

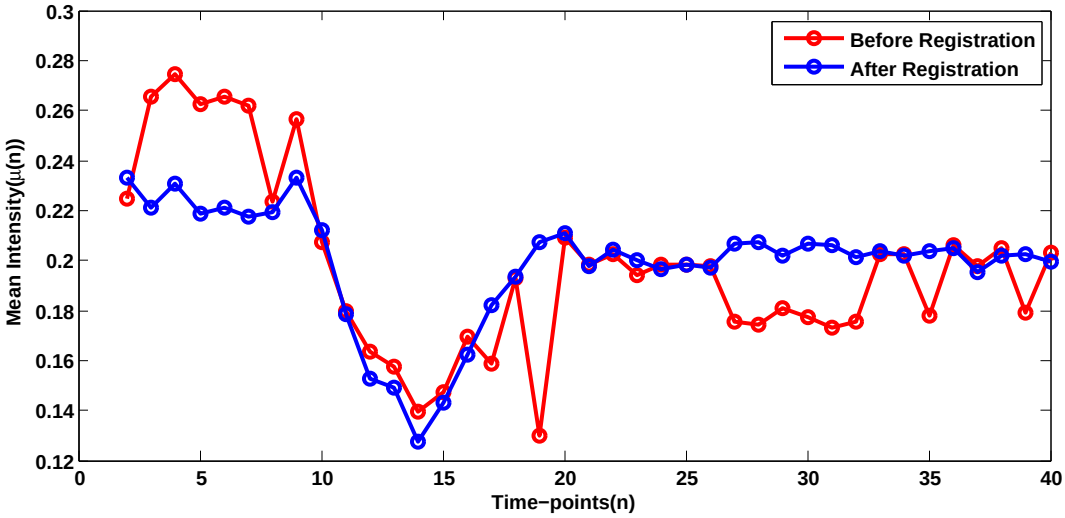

Figure 6.8 Mean-Intensity Plot of a volumetric region in a DSC-MRI time-series.

Table 6.2 Evaluation of our approach in terms of registration error and computation cost.

Total no. of Volumes	No. of corrupt Volumes	Rotation in R_x (degrees)	Rotation in R_z (degrees)	Registration Method	No. of Corrupt Volumes Detected	Regn. Error (e_{rms})	Time Taken (min)
39	25	[0 10]	[-10 10]	MI based	NA	0.28	26.83
				Our approach	21	**0.22**	**13.64**
39	25	[0 10]	[-15 15]	MI based	NA	0.60	30.17
				Our approach	24	**0.37**	**17.62**
39	25	[0 10]	[-20 20]	MI based	NA	0.54	27.58
				Our approach	22	**0.34**	**14.90**

registration method[30] for different degrees of rotation. A number of points can be noted from the tabulated results. Firstly, the motion detection step applied prior to motion correction helps reject the stationary volumes from the time-series. Thus, only a subset of volumes is corrected in our approach as compared to traditional approaches that register all the volumes in the time-series to a mean volume. The success in detecting motion-corrupted volumes was generally found to be lower for small rotation angles. This is primarily due to the block size chosen in the phase correlation. The randomness in generation of rotation angles meant that even for large range of motion ([-20° 20°]), the actual angle of rotation added to a volume could be small, thus resulting in a lower number of correct detection. Second, the registration error (e_{rms}) in our approach is consistently lower than that for the MI based approach. An increase in amount of rotation in R_z direction results in an increase in error for both methods but the increase is less for our method. Lastly, the time taken for correction of entire time-series with our approach is less. This is both due to MI based methods being computationally intensive and that the number of volumes being corrected is also higher. The time taken (for detection and correction) can be reduced further by using a multicore architecture built in C++.

6.7 Summary

We present an efficient 2-pass registration for alignment of motion-corrupt volumes in brain DSC-MRI. Some features e.g. edges that appear after wash-in of contrast agent in brain are absent before the wash-in period. Hence, any correction algorithm based on those features is likely to fail as it assumes that the features remain same across the time-points. We are able to overcome this obstacle by dividing the entire time-series into three classes of before, during and after passage of bolus through brain. This ensures that the features in the same set remain similar. Thus, an intra-set registration in the first pass of registration makes the approach more accurate. The inter-set registration which is the final registration of reference volumes between two sets results in a reduction of the overhead in the number of transformations that are required to be estimated.

One can argue that after applying GVF fitting to volumes after wash-in period, the corrupted volumes can be registered to a pre-wash-in volume via intensity correction. Though this would result in estimating less number of transformations, we avoided the approach since it could result in a decrease in accuracy of registration. GVF fitting provides an approximate model of intensity variation after the wash-in period. Thus, the error in registration due to intensity correction with GVF fitting would increase with an increase in the number of corrupted volumes after wash-in period.

The computational time for the algorithm can be reduced significantly by implementing the algorithm on a multicore architecture [51] using C++.

Chapter 7

Discussion and Conclusion

Patient motion corrupts the acquired MR scans. The problem becomes more emphatic in perfusion MR scans due to their longer acquisition times. We aimed at solving the problem of motion corruption due to patient motion in DSC-MRI in an efficient manner. It is important that the motion is removed first so that the acquired images can be used later for diagnostic purposes. Existing techniques of motion correction consist of aligning all the volumes in the time-series to a reference volume via 3D registration. 3D registration is a computationally intensive task. Employing such a method on all the volumes proves to be costly. In this thesis, we presented a fast and efficient system for motion correction in 3D DSC-MRI time-series of brain.

To overcome the problems faced by existing methods, we developed a multi-stage motion correction system based on divide and conquer strategy. Depending on the status of bolus in brain, we divided the DSC-MRI times-series into different sets using gamma-variate-function fitting. Next, we detected the presence of motion in volumes using a method based on block-wise phase correlation and also categorized the volumes into different categories depending on the degrees of motion. Finally, we removed the motion present in volumes using a two-pass registration scheme. The motion detection and correction stages employed an intensity correction technique to mitigate the effects of variation in contrast due to injected bolus.

In the previous chapters, we demonstrated the accuracies of our motion detection and motion correction methods. In this chapter, we evaluate the system in terms of computation time required for motion correction. First, we show the reduction in computational time achieved by our motion detection method by applying it prior to existing motion correction methods. Next, we will show the overall reduction in time achieved by our system.

Existing techniques do not use a motion detection strategy in the correction pipeline for perfusion weighted MRI. However, we argue that motion detection prior to correction can lighten the load for the correction stage. We demonstrate this by estimating the reduction in time that can be achieved by

Table 7.1 Effect of motion detection on computation time when applied prior to existing motion detection algorithms.

Motion Correction Method	**Time taken to correct (N-1) volumes ($\mathbf{t_{old}}$ (sec))**	**Mean Time per volume registration $\mathbf{t_m = t_{old}/(N-1)}$ (sec)**	**Time taken to correct $\mathbf{N_{md}}$ volumes (sec)**	**Reduction in time $\mathbf{t_{old} - t_{new}}$ (sec)**	**Percentage Time Reduction** ($\%$)
[29]	640.39	16.42	397.42	242.97	**37.94**
[51]	636.38	16.32	395.74	240.64	**37.81**
[52]	1018.20	26.11	668.78	349.42	**34.32**

including our detection as a front end to existing motion correction algorithms. Motion correction via 3D image registration methods is a standard approach followed by existing methods. This serves to align volumes in the given time-series to a chosen reference volume [29][51][52]. For the purpose of our study, the volume at time-point n=2 is chosen as the reference volume (F_R). All the remaining volumes in the time-series are registered to this reference volume. Table 7.1 shows the time taken by some existing methods of motion correction algorithms for perfusion weighted MRI. In our DSC-MRI time-series data of $N = 40$ volumes, motion was added to $N_1 = 16$ volumes. However, this was done only to $m = 3$ blocks of contiguous volumes (please refer to Figure 5.5 in Chapter 5).

Initially, all the remaining $N - 1 = 39$ volumes are registered to reference volume F_R. With motion detection, the number of volumes that need to be registered reduces to $N_{md} = 23$ $((N - 1) - N_1 + m)$ thereby reducing the time taken for motion correction. Since the volumes in each of these $m = 3$ intervals undergo same degree of motion, only one volume in each interval needs to be aligned. This results in a reduction in time taken for motion correction. From the results, it can be seen that a considerable reduction in time is achieved with percentage as high as $\mathbf{37.94}\%$. In Table 7.1, time taken for motion correction with motion detection (t_{new}) is reported for motion correction stage only since the time taken for motion detection (7.68 sec) is negligible compared to the time required for registration.
Table 7.2 shows time taken by our system for correcting motion in a DSC-MRI time-series. From the results, it can be seen that a considerable reduction in the meantime is achieved by our system as compared to existing methods which is as high as 73.22%.

The analysis of the system shows that it can detect the presence of motion in the time-series, accurately correct the time-series corrupted by different degrees of motion and achieve a reduction in computation time that is as high as 73.22%. We can see that there is no trade-off between the accuracy and computation time of our system. Hence, the analysis of the system shows that it is fast and efficient.

Table 7.2 Comparison of our motion correction system with existing motion correction methods in terms of computation time.

Motion Correction Method	Time for motion detection (sec)	Time for motion correction(sec)	Total Time (sec)	Mean Time (sec)	Percentage Time reduction (%)
[29]	NA	640.39	640.39	16.42	57.43
[51]	NA	636.38	636.38	16.31	57.14
[52]	NA	1018.20	1018.20	26.10	73.22
Our Approach	7.68	264.59	272.97	**6.99**	-

7.1 Issues faced

- Perfusion MR scan is not a common practice in medical centres. Hence, acquiring perfusion MR data proved to be a difficult task in this framework.
- Motion corrupted perfusion MRI dataset was not available. Hence, the patient motion was simulated in the dataset by applying rigid transformations to the original dataset.
- Choosing a suitable slice resolution and block size during motion detection was difficult. On decreasing the resolution, small amounts of motion were overlooked by the algorithm. For a particular resolution, choosing a large block size resulted in a complete miss of the patient motion. These parameters were chosen empirically.
- It is assumed that the motion found in the central slice represents the motion for entire volume. This assumption is valid for cases where image acquisition is fast.

In spite of these problems, the proposed motion correction system shows promising results. The advantage of a fast motion detection system in the data acquisition pipeline is that feedback can be provided to the scanner console operator on presence so that appropriate action can be taken. In the absence of an online motion detection stage, once the data has been acquired, it can be corrected for motion using the presented system. The advantage of such a system is that it does not required human intervention and is completely automated.

In this thesis, we looked at a problem that lurks in the data acquisition stage of a big pipeline. By acquiring knowledge about the field and using image analysis methods, solutions to handle this problem have been proposed over the years, each one taking advantage of the research and developments made during that period. Overall, it can be concluded that advancements in clinical research along with the developments of new methods and technologies not only help in diagnosis and treatment of diseases but also pave path for new and better solutions to these problems.

7.2 Future Work

Future work in the area can be aimed at solving the above mentioned problems.

- A hierarchical automated method for choosing a suitable slice resolution and block size for fast motion detection can solve the problem of selecting these parameters empirically, although this will increase the time used in motion detection.
- Methods alternate to block-wise phase correlation can be used for detecting motion between volumes keeping in mind the boundaries of motion.
- The motion detection method is based on assumption that the central slice represents the motion for the entire volume. This is true, since the acquisition time for a single volume is very low. Clearly, a method for detecting motion that is independent of this assumption would be a better choice.
- After categorizing the motion into different categories, the presented system deploys same method for motion correction irrespective of the degree to which the time-series is corrupted. Different motion correction methods can be employed for correcting motion in these categories.
- The proposed system has been evaluated on real data with simulated motion. Even though we have kept the limits to model a real scenario, it would be interesting to see how the system performs in a real scenario of motion corruption.

Appendix A

Appendix

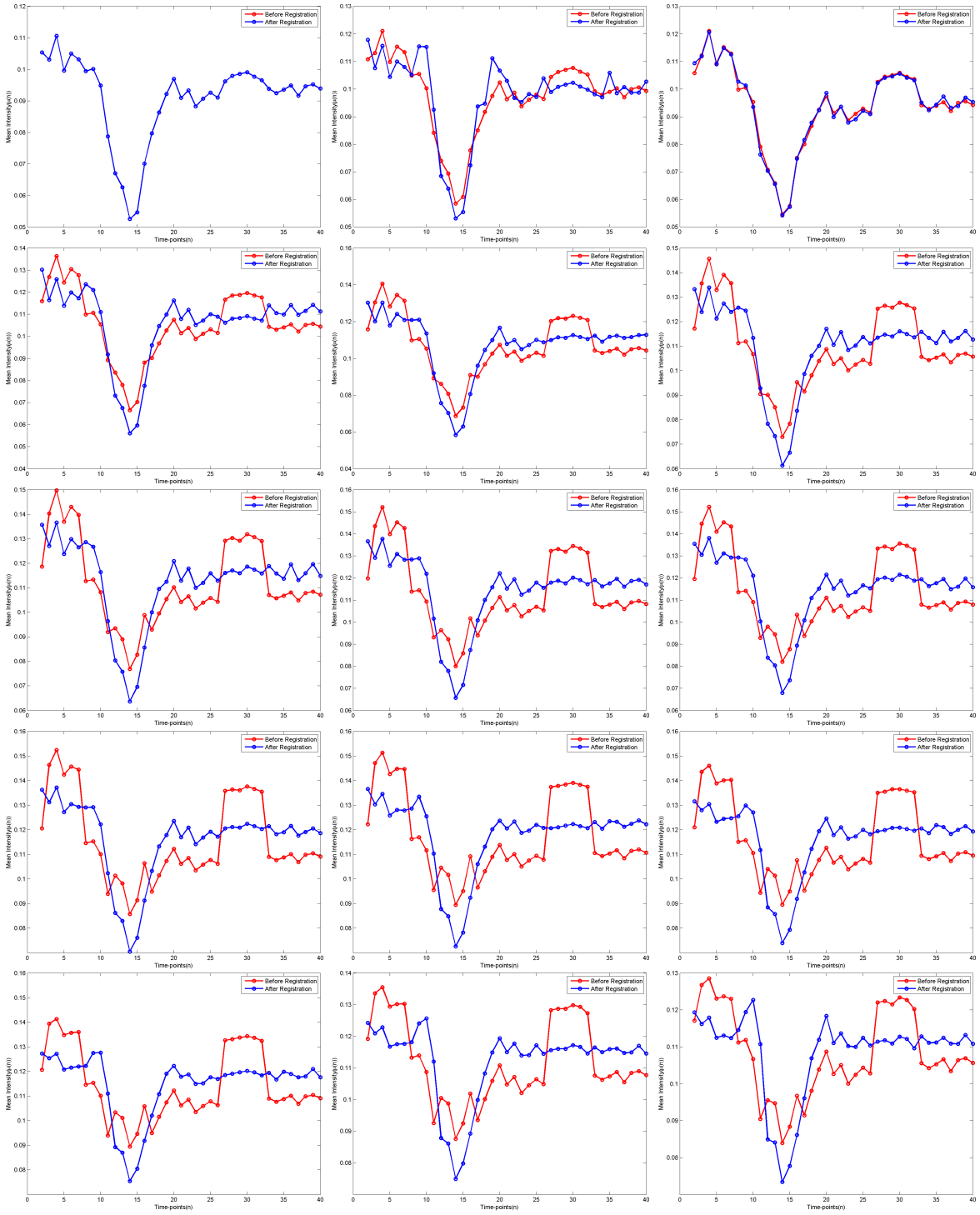

Figure A.1 Mean Intensity plot of a manually selected volumetric region before and after motion correction for various degrees of motion. The angle of rotation increases from left to right and top to bottom in the range $[0°, 15°]$ in transverse direction (R_z).

Related Publications

- R. Gautam, J. Sivaswamy and R. Varma. **An efficient, bolus-stage based method for motion correction in perfusion weighted MRI**. In *Proceedings of the 21st International Conference on Pattern Recognition*, Tsukuba Science City, Japan, 2012.
- R. Gautam, J. Sivaswamy and R. Varma. **A method for motion detection and categorization in perfusion weighted MRI**. In *Proceedings of the Eighth Indian Conference on Computer Vision, Graphics and Image Processing*, Mumbai, India, 2012.

Bibliography

[1] Radiology assistant. http://www.radiologyassistant.nl.

[2] G. Adluru, E. DiBella, and M. Schabel. Model-based registration for dynamic cardiac perfusion mri. *Journal of Magnetic Resonance Imaging*, 24(5):1062–1070, 2006.

[3] M. Ahmed, S. Yamany, N. Mohamed, A. Farag, and T. Moriarty. A modified fuzzy c-means algorithm for bias field estimation and segmentation of mri data. *Medical Imaging, IEEE Transactions on*, 21(3):193–199, 2002.

[4] J. Akre. A genetic predisposition to stroke discovered, 2009.

[5] E. Ardizzone, R. Pirrone, and O. Gambino. Fuzzy c-means segmentation on brain mr slices corrupted by rf-inhomogeneity. *Applications of Fuzzy Sets Theory*, pages 378–384, 2007.

[6] J. Astrup, B. K. Siesj, and L. Symon. Thresholds in cerebral ischemia - the ischemic penumbra. *Stroke*, 12(6):723–5, 1981.

[7] J. Belliveau, B. Rosen, H. Kantor, R. Rzedzian, D. Kennedy, R. McKinstry, J. Vevea, M. Cohen, I. Pykett, and T. Brady. Functional cerebral imaging by susceptibility-contrast nmr. *Magnetic Resonance in Medicine*, 14(3):538–546, 2005.

[8] J. Bezdek, R. Ehrlich, and W. Full. Fcm: The fuzzy c-means clustering algorithm. *Computers & Geosciences*, 10(2):191–203, 1984.

[9] J. Bezdek and S. Pal. *Fuzzy models for pattern recognition*, volume 23. IEEE press New York, 1992.

[10] J. Bican and J. Flusser. 3d rigid registration by cylindrical phase correlation method. *Pattern Recogn. Lett.*, 30:914–921, July 2009.

[11] M. Brown, R. Semelka, and T. K. Nishino. Mri: basic principles and applications. *Medical Physics-New York-Institute of Physics*, 31(1):170, 2004.

[12] G. Buonaccorsi, C. Roberts, S. Cheung, Y. Watson, K. Davies, A. Jackson, G. Jayson, and G. Parker. Tracer kinetic model-driven registration for dynamic contrast-enhanced mri time-series data. *Magnetic Resonance in Medicine*, 58(5):1010–1019, 2007.

[13] I. Carlbom, D. Terzopoulos, and K. Harris. Computer-assisted registration, segmentation, and 3d reconstruction from images of neuronal tissue sections. *Medical Imaging, IEEE Transactions on*, 13(2):351–362, 1994.

[14] A. Chakraborty, L. Staib, and J. Duncan. An integrated approach for surface finding in medical images. In *Mathematical Methods in Biomedical Image Analysis, 1996., Proceedings of the Workshop on*, pages 253–262. IEEE, 1996.

[15] J. A. Chalela, C. S. Kidwell, L. M. Nentwich, M. Luby, J. A. Butman, A. M. Demchuk, M. D. Hill, N. Patronas, L. Latour, and S. Warach. Magnetic resonance imaging and computed tomography in emergency assessment of patients with suspected acute stroke: a prospective comparison. *The Lancet*, 369(9558):293–298, 2007.

[16] A. A. Chan and S. Nelson. Simplified gamma-variate fitting of perfusion curves. *International Symposium on Biomedical Imaging*, 2(2):1067–1070, 2004.

[17] K. Chuang, H. Tzeng, S. Chen, J. Wu, and T. Chen. Fuzzy c-means clustering with spatial information for image segmentation. *computerized medical imaging and graphics*, 30(1):9–15, 2006.

[18] A. Collignon, F. Maes, D. Delaere, D. Vandermeulen, P. Suetens, and G. Marchal. Automated multi-modality image registration based on information theory. In *Information processing in medical imaging*, volume 3, pages 264–274, 1995.

[19] J. Den Boer and P. Folkers. Mr perfusion and diffusion imaging in ischaemic brain disease. *medicamundi*, 41:20–35, 1997.

[20] A. El-Baz, G. Gimel'farb, and M. El-Ghar. New motion correction models for automatic identification of renal transplant rejection. In *Proceedings of the 10th international conference on Medical image computing and computer-assisted intervention*, MICCAI'07, pages 235–243, Berlin, Heidelberg, 2007. Springer-Verlag.

[21] C. Grandin. Assessment of brain perfusion with mri: methodology and application to acute stroke. *Neuroradiology*, 45:755–766, 2003.

[22] J. Hajnal, N. Saeed, E. Soar, A. Oatridge, I. Young, G. Bydder, et al. A registration and interpolation procedure for subvoxel matching of serially acquired mr images. *Journal of computer assisted tomography*, 19(2):289, 1995.

[23] J. Head and M. Zerner. A broyden-fletcher-goldfarb-shanno optimization procedure for molecular geometries. *Chemical physics letters*, 122(3):264–270, 1985.

[24] D. Hill, P. Batchelor, M. Holden, and D. Hawkes. Medical image registration. *Physics in medicine and biology*, 46(3):R1, 2001.

[25] D. L. Hill, C. Studholme, and D. J. Hawkes. Voxel similarity measures for automated image registration. In *Visualization in Biomedical Computing 1994*, pages 205–216. International Society for Optics and Photonics, 1994.

[26] M. Jenkinson, P. Bannister, M. Brady, and S. Smith. Improved optimization for the robust and accurate linear registration and motion correction of brain images. *NeuroImage*, 17(2):825–841, 2002.

[27] M. Kim, G. Wu, and D. Shen. Groupwise registration of breast dce-mr images for accurate tumor measurement. In *IEEE International Symposium on Biomedical Imaging*, pages 598 –601, 2011.

[28] K. Kohsuke. Perfusion mismatch analyzer. `http://asist.umin.jp/index-e.htm`, 2011.

[29] R. Kosior, J. Kosior, and R. Frayne. Improved dynamic susceptibility contrast (dsc)-mr perfusion estimates by motion correction. *Journal of Magnetic Resonance Imaging*, 26(4):1167–1172, 2007.

[30] D. Kroon and C. Slump. Mri modalitiy transformation in demon registration. In *Biomedical Imaging: From Nano to Macro, 2009. ISBI'09. IEEE International Symposium on*, pages 963–966. IEEE, 2009.

[31] C. Kuglin. The phase correlation image alignment methed. In *Proc. Int. Conference Cybernetics Society*, pages 163–165, 1975.

[32] A. Lausch, M. Ebrahimi, and A. L. Martel. Image registration for abdominal dynamic contrast-enhanced magnetic resonance images. In *International Symposium on Biomedical Imaging*, pages 561–565. IEEE, 2011.

[33] H. Lester and S. Arridge. A survey of hierarchical non-linear medical image registration. *Pattern recognition*, 32(1):129–149, 1999.

[34] M. Madsen. A simplified formulation of the gamma variate function. *Physics in Medicine and Biology*, 37(7):1597, 2000.

[35] F. Maes, A. Collignon, D. Vandermeulen, G. Marchal, and P. Suetens. Multimodality image registration by maximization of mutual information. *Medical Imaging, IEEE Transactions on*, 16(2):187–198, 1997.

[36] P. Meier and K. Zierler. On the theory of the indicator-dilution method for measurement of blood flow and volume. *Journal of applied physiology*, 6(12):731–744, 1954.

[37] A. Melbourne, D. Atkinson, M. White, D. Collins, M. Leach, and D. Hawkes. Registration of dynamic contrast-enhanced MRI using a progressive principal component registration (PPCR). *Physics in Medicine and Biology*, 52(17):5147–5156, Sept. 2007.

[38] J. Nocedal and S. Wright. *Numerical optimization*. Springer verlag, 1999.

[39] R. Nock and F. Nielsen. On weighting clustering. *Pattern Analysis and Machine Intelligence, IEEE Transactions on*, 28(8):1223–1235, 2006.

[40] L. Ostergaard. Cerebral perfusion imaging by bolus tracking. *Topics in magnetic resonance imaging TMRI*, 15(1):3–9, 2004.

[41] J. Perkiö, H. Aronen, A. Kangasmäki, Y. Liu, J. Karonen, S. Savolainen, and L. Østergaard. Evaluation of four postprocessing methods for determination of cerebral blood volume and mean transit time by dynamic susceptibility contrast imaging. *Magnetic resonance in medicine*, 47(5):973–981, 2002.

[42] J. Petrella and J. Provenzale. Mr perfusion imaging of the brain techniques and applications. *American Journal of Roentgenology*, 175(1):207–219, 2000.

[43] A. Roche, G. Malandain, X. Pennec, and N. Ayache. The correlation ratio as a new similarity measure for multimodal image registration. *Medical Image Computing and Computer-Assisted InterventationMICCAI98*, pages 1115–1124, 1998.

[44] P. Rogelj, S. Kovacic, and J. Gee. Validation of a nonrigid registration algorithm for multimodal data. *Medical Imaging*, 4684:299–307, 2002.

[45] B. Rosen, J. Belliveau, H. Aronen, D. Kennedy, B. Buchbinder, A. Fischman, M. Gruber, J. Glas, R. Weisskoff, M. Cohen, et al. Susceptibility contrast imaging of cerebral blood volume: human experience. *Magnetic Resonance in Medicine*, 22(2):293–299, 2005.

[46] B. Rosen, J. Belliveau, B. Buchbinder, R. McKinstry, L. Porkka, D. Kennedy, M. Neuder, C. Fisel, H. Aronen, K. Kwong, et al. Contrast agents and cerebral hemodynamics. *Magnetic resonance in medicine*, 19(2):285–292, 1991.

[47] B. Rosen, J. Belliveau, J. Vevea, and T. Brady. Perfusion imaging with nmr contrast agents. *Magnetic resonance in medicine*, 14(2):249–265, 2005.

[48] H. Seo and P. Milanfar. A non-parametric approach to automatic change detection in mri images of the brain. In *Biomedical Imaging: From Nano to Macro, 2009. ISBI'09. IEEE International Symposium on*, pages 245–248. IEEE, 2009.

[49] D. Shanbhag, R. Mullick, S. Nath, C. Oppenheim, M. Luby, K. Ku, L. Latour, S. Warach, and N. Natural. Impact of motion and symmetry correction on perfusion lesion segmentation in acute ischemic stroke : Quantitative evaluation. *Brain*, 17:4710–4710, 2009.

[50] G. Stewart. Researches on the circulation time in organs and on the influences which affect it: Parts i.iii. *The Journal of Physiology*, 15(1-2):1, 1893.

[51] M. Straka, G. Albers, and R. Bammer. Real-time diffusion-perfusion mismatch analysis in acute stroke. *Journal of Magnetic Resonance Imaging*, 32(5):1024–1037, 2010.

[52] C. Tanner, J. Schnabel, D. Chung, M. Clarkson, D. Rueckert, D. Hill, and D. Hawkes. Volume and shape preservation of enhancing lesions when applying non-rigid registration to a time series of contrast enhancing mr breast images. In *Medical Image Computing and Computer-Assisted Intervention, MICCAI 2000*.

[53] S. Thiruvenkadam, S. Arcot, and C. Yunmei. A pde based method for fuzzy classification of medical images. In *IEEE International Conference on Image Processing, 2006*, pages 1805 –1808, oct. 2006.

[54] J. Tokuda, H. Mamata, R. Gill, N. Hata, R. Kikinis, R. Padera, R. Lenkinski, D. Sugarbaker, and H. Hatabu. Impact of nonrigid motion correction technique on pixel-wise pharmacokinetic analysis of free-breathing pulmonary dynamic contrast-enhanced mr imaging. *Journal of Magnetic Resonance Imaging*, 33(4):968–973, 2011.

[55] A. Villringer, B. Rosen, J. Belliveau, J. Ackerman, R. Lauffer, R. Buxton, Y. Chao, V. Wedeenand, and T. Brady. Dynamic imaging with lanthanide chelates in normal brain: contrast due to magnetic susceptibility effects. *Magnetic resonance in medicine*, 6(2):164–174, 2005.

[56] P. Viola and W. Wells III. Alignment by maximization of mutual information. *International journal of computer vision*, 24(2):137–154, 1997.

[57] W. Wells, P. Viola, H. Atsumi, S. Nakajima, and R. Kikinis. Multi-modal volume registration by maximization of mutual information. *Medical image analysis*, 1(1):35–51, 1996.

[58] C. Xiaohua, M. Brady, J. Lo, and N. Moore. Simultaneous segmentation and registration of contrast-enhanced breast mri. In *Information Processing in Medical Imaging*, pages 31–59. Springer, 2005.

[59] T. Yoo. *Insight into images: principles and practice for segmentation, registration, and image analysis*, volume 203. AK Peters Wesllesleyˆ eMassachusetts Massachusetts, 2004.

[60] Y. Zheng, A. Maidment, and J. Gee. Accurate registration of dynamic contrast-enhanced breast mr images with robust estimation and linear programming. In *Biomedical Imaging: From Nano to Macro, 2010 IEEE International Symposium on*, pages 536–539. IEEE, 2010.

[61] B. Zitova and J. Flusser. Image registration methods: a survey. *Image and vision computing*, 21(11):977–1000, 2003.

[62] F. Zöllner, R. Sance, P. Rogelj, M. Ledesma-Carbayo, J. Rørvik, A. Santos, and A. Lundervold. Assessment of 3d dce-mri of the kidneys using non-rigid image registration and segmentation of voxel time courses. *Computerized Medical Imaging and Graphics*, 33(3):171–181, 2009.